



TOI-1235 b: A Keystone Super-Earth for Testing Radius Valley Emergence Models around Early M Dwarfs

Ryan Cloutier¹ , Joseph E. Rodriguez¹ , Jonathan Irwin¹, David Charbonneau¹ , Keivan G. Stassun² , Annelies Mortier³ , David W. Latham¹ , Howard Isaacson^{4,5} , Andrew W. Howard⁶ , Stéphane Udry⁷ , Thomas G. Wilson⁸, Christopher A. Watson⁹, Matteo Pinamonti¹⁰, Florian Lienhard³, Paolo Giacobbe¹⁰, Pere Guerra¹¹, Karen A. Collins¹ , Allyson Beiryla¹ , Gilbert A. Esquerdo¹ , Elisabeth Matthews¹² , Rachel A. Matson¹³ , Steve B. Howell¹⁴ , Elise Furlan¹⁵, Ian J. M. Crossfield¹⁶, Jennifer G. Winters¹ , Chantanelle Nava¹ , Kristo Ment¹ , Eric D. Lopez^{17,18}, George Ricker¹² , Roland Vanderspek¹² , Sara Seager^{19,20,21} , Jon M. Jenkins¹⁴ , Eric B. Ting¹⁴ , Peter Tenenbaum¹⁴ , Alessandro Sozzetti¹⁰ , Lizhou Sha¹⁹ , Damien Ségransan⁷ , Joshua E. Schlieder¹⁷ , Dimitar Sasselov¹ , Arpita Roy⁶ , Paul Robertson²² , Ken Rice²³, Ennio Poretti^{24,25} , Giampaolo Piotto²⁶ , David Phillips¹, Joshua Pepper²⁷ , Francesco Pepe⁷, Emilio Molinari²⁸ , Teo Mocnik²⁹ , Giuseppina Micela³⁰ , Michel Mayor⁷, Aldo F. Martinez Fiorenzano²⁴, Franco Mallia³¹, Jack Lubin²² , Christophe Lovis⁷, Mercedes López-Morales¹ , Molly R. Kosiarek³², John F. Kielkopf³³ , Stephen R. Kane³⁴ , Eric L. N. Jensen³⁵ , Giovanni Isopi³¹, Daniel Huber³⁶ , Michelle L. Hill³⁴ , Avet Harutyunyan²⁴, Erica Gonzales³², Steven Giacalone⁴ , Adriano Ghedina²⁴ , Andrea Ercolino³¹, Xavier Dumusque⁷ , Courtney D. Dressing⁴ , Mario Damasso¹⁰, Paul A. Dalba^{34,44} , Rosario Cosentino²⁴ , Dennis M. Conti³⁷ , Knicole D. Colón³⁸ , Kevin I. Collins³⁹ , Andrew Collier Cameron⁸, David Ciardi¹⁵ , Jessie Christiansen¹⁵ , Ashley Chontos^{36,45} , Massimo Cecconi²⁴, Douglas A. Caldwell¹⁴ , Christopher Burke⁴⁰ , Lars Buchhave⁴¹ , Charles Beichman⁴², Aida Behmard^{43,45} , Corey Beard²² , and Joseph M. Akana Murphy^{32,45}

¹ Center for Astrophysics | Harvard & Smithsonian, 60 Garden Street, Cambridge, MA 02138, USA; ryan.cloutier@cfa.harvard.edu

² Department of Physics & Astronomy, Vanderbilt University, 6301 Stevenson Center Lane, Nashville, TN 37235, USA

³ Astrophysics Group, Cavendish Laboratory, University of Cambridge, J.J. Thomson Avenue, Cambridge CB3 0HE, UK

⁴ 501 Campbell Hall, University of California at Berkeley, Berkeley, CA 94720, USA

⁵ Centre for Astrophysics, University of Southern Queensland, Toowoomba, QLD, Australia

⁶ Department of Astronomy, California Institute of Technology, Pasadena, CA 91125, USA

⁷ Observatoire Astronomique de l'Université de Genève, 51 chemin des Maillettes, 1290 Versoix, Switzerland

⁸ School of Physics and Astronomy, University of St Andrews, North Haugh, St Andrews, Fife, KY16 9SS, UK

⁹ Astrophysics Research Centre, School of Mathematics and Physics, Queen's University Belfast, Belfast, BT7 1NN, UK

¹⁰ INAF—Osservatorio Astrofisico di Torino, Strada Osservatorio 20, Pino Torinese (To) I-10025, Italy

¹¹ Observatori Astronòmic Albanyà, Camí de Bassegoda S/N, Albanyà E-17733, Girona, Spain

¹² Department of Earth, Atmospheric and Planetary Sciences, and Kavli Institute for Astrophysics and Space Research, Massachusetts Institute of Technology, Cambridge, MA 02139, USA

¹³ U.S. Naval Observatory, Washington, DC 20392, USA

¹⁴ NASA Ames Research Center, Moffett Field, CA 94035, USA

¹⁵ Caltech/IPAC, 1200 E. California Blvd., Pasadena, CA 91125, USA

¹⁶ Department of Physics & Astronomy, University of Kansas, 1082 Malott, 1251 Wescoe Hall Dr., Lawrence, KS 66045, USA

¹⁷ NASA Goddard Space Flight Center, 8800 Greenbelt Rd., Greenbelt, MD 20771, USA

¹⁸ GSFC Sellers Exoplanet Environments Collaboration, NASA Goddard Space Flight Center, Greenbelt, MD 20771, USA

¹⁹ Department of Physics and Kavli Institute for Astrophysics and Space Research, Massachusetts Institute of Technology, Cambridge, MA 02139, USA

²⁰ Department of Earth, Atmospheric and Planetary Sciences, Massachusetts Institute of Technology, Cambridge, MA 02139, USA

²¹ Department of Aeronautics and Astronautics, MIT, 77 Massachusetts Avenue, Cambridge, MA 02139, USA

²² Department of Physics & Astronomy, University of California Irvine, Irvine, CA 92697, USA

²³ SUPA, Institute for Astronomy, University of Edinburgh, Blackford Hill, Edinburgh, EH9 3HJ, Scotland, UK

²⁴ Fundación Galileo Galilei-IAF, Rambla José Ana Fernández Pérez 7, E-38712 Breña Baja, TF, Spain

²⁵ INAF—Osservatorio Astronomico di Brera, via E. Bianchi 46, I-23807 Merate (LC), Italy

²⁶ Dip. di Fisica e Astronomia Galileo Galilei—Università di Padova, Vicolo dell'Osservatorio 2, I-35122, Padova, Italy

²⁷ Lehigh University, Department of Physics, 16 Memorial Drive East, Bethlehem, PA 18015, USA

²⁸ INAF—Osservatorio Astronomico di Cagliari, via della Scienza 5, I-09047, Selargius, Italy

²⁹ Gemini Observatory Northern Operations, 670 N. A'ohoku Place, Hilo, HI 96720, USA

³⁰ INAF—Osservatorio Astronomico di Palermo, Piazza del Parlamento 1, I-90134 Palermo, Italy

³¹ Campo Catino Astronomical Observatory, Regione Lazio, Guarcino (FR), I-03010, Italy

³² Department of Astronomy and Astrophysics, University of California, Santa Cruz, CA 95064, USA

³³ Department of Physics and Astronomy, University of Louisville, Louisville, KY 40292, USA

³⁴ Department of Earth and Planetary Sciences, University of California, Riverside, CA 92521, USA

³⁵ Dept. of Physics & Astronomy, Swarthmore College, Swarthmore, PA 19081, USA

³⁶ Institute for Astronomy, University of Hawai'i, 2680 Woodlawn Drive, Honolulu, HI 96822, USA

³⁷ American Association of Variable Star Observers, 49 Bay State Road, Cambridge, MA 02138, USA

³⁸ NASA Goddard Space Flight Center, Exoplanets and Stellar Astrophysics Laboratory (Code 667), Greenbelt, MD 20771, USA

³⁹ George Mason University, 4400 University Drive, Fairfax, VA 22030, USA

⁴⁰ Kavli Institute for Astrophysics and Space Research, Massachusetts Institute of Technology, Cambridge, MA 02139, USA

⁴¹ DTU Space, National Space Institute, Technical University of Denmark, Elektrovej 328, DK-2800 Kgs. Lyngby, Denmark

⁴² NASA Exoplanet Science Institute, Infrared Processing & Analysis Center, Jet Propulsion Laboratory, California Institute of Technology, Pasadena CA 91125, USA

⁴³ Division of Geological and Planetary Science, California Institute of Technology, Pasadena, CA 91125, USA

Received 2020 April 13; revised 2020 May 13; accepted 2020 May 19; published 2020 June 12

⁴⁴ NSF Astronomy and Astrophysics Postdoctoral Fellow.

⁴⁵ NSF Graduate Research Fellow.

Abstract

Small planets on close-in orbits tend to exhibit envelope mass fractions of either effectively zero or up to a few percent depending on their size and orbital period. Models of thermally driven atmospheric mass loss and of terrestrial planet formation in a gas-poor environment make distinct predictions regarding the location of this rocky/nonrocky transition in period–radius space. Here we present the confirmation of TOI-1235 b ($P = 3.44$ days, $r_p = 1.738^{+0.087}_{-0.076} R_\oplus$), a planet whose size and period are intermediate between the competing model predictions, thus making the system an important test case for emergence models of the rocky/nonrocky transition around early M dwarfs ($R_s = 0.630 \pm 0.015 R_\odot$, $M_s = 0.640 \pm 0.016 M_\odot$). We confirm the TESS planet discovery using reconnaissance spectroscopy, ground-based photometry, high-resolution imaging, and a set of 38 precise radial velocities (RVs) from HARPS-N and HIRES. We measure a planet mass of $6.91^{+0.75}_{-0.85} M_\oplus$, which implies an iron core mass fraction of $20^{+15}_{-12}\%$ in the absence of a gaseous envelope. The bulk composition of TOI-1235 b is therefore consistent with being Earth-like, and we constrain an H/He envelope mass fraction to be $<0.5\%$ at 90% confidence. Our results are consistent with model predictions from thermally driven atmospheric mass loss but not with gas-poor formation, suggesting that the former class of processes remains efficient at sculpting close-in planets around early M dwarfs. Our RV analysis also reveals a strong periodicity close to the first harmonic of the photometrically determined stellar rotation period that we treat as stellar activity, despite other lines of evidence favoring a planetary origin ($P = 21.8^{+0.9}_{-0.8}$ days, $m_p \sin i = 13.0^{+3.8}_{-5.3} M_\oplus$) that cannot be firmly ruled out by our data.

Unified Astronomy Thesaurus concepts: Radial velocity (1332); M dwarf stars (982); Transit photometry (1709); Exoplanet formation (492); Exoplanet structure (495)

Supporting material: data behind figure, machine-readable table

1. Introduction

The occurrence rate distribution of close-in planets features a dearth of planets between 1.7 and $2.0 R_\oplus$ around Sun-like stars ($T_{\text{eff}} > 4700$ K; Fulton et al. 2017; Fulton & Petigura 2018; Mayo et al. 2018) and between 1.4 and $1.7 R_\oplus$ around mid-K to mid-M dwarfs ($T_{\text{eff}} < 4700$ K; Cloutier & Menou 2020). The so-called radius valley likely emerges as a result of the existence of a transition from primarily rocky planets to larger nonrocky planets that host extended H/He envelopes up to a few percent by mass (Weiss & Marcy 2014; Dressing et al. 2015; Rogers 2015). Furthermore, the exact location of the rocky/nonrocky transition around both Sun-like and lower-mass stars is known to be period dependent (van Eylen et al. 2018; Martinez et al. 2019; Wu 2019; Cloutier & Menou 2020), with the model-predicted slope of the period dependence varying between competing physical models that describe potential pathways for the radius valley’s emergence. One class of models relies on thermal heating to drive atmospheric escape. For example, photoevaporation, wherein a planet’s primordial atmosphere is stripped by X-ray and UV photons from the host star during the first 100 Myr (Owen & Wu 2013; Jin et al. 2014; Lopez & Fortney 2014; Chen & Rogers 2016; Owen & Wu 2017; Jin & Mordasini 2018; Lopez & Rice 2018; Wu 2019), predicts that the slope of the radius valley should vary with orbital period as $r_{p,\text{valley}} \propto P^{-0.15}$ (Lopez & Rice 2018). A similar slope of $r_{p,\text{valley}} \propto P^{-0.13}$ (Gupta & Schlichting 2020) is predicted by internally driven thermal atmospheric escape models via the core-powered mass-loss mechanism (Ginzburg et al. 2018; Gupta & Schlichting 2019, 2020). However, if instead the radius valley emerges from the superposition of rocky and nonrocky planet populations, wherein the former are formed at late times in a gas-poor environment (Lee et al. 2014; Lee & Chiang 2016; Lopez & Rice 2018), then the period dependence of the radius valley should have the opposite sign: $r_{p,\text{valley}} \propto P^{0.11}$ (Lopez & Rice 2018). These distinct slope predictions naturally carve out a subspace in period–radius space wherein knowledge of planetary bulk compositions can directly constrain the applicability of each class of model (Figure 15, Cloutier & Menou 2020, hereafter CM19). This is because within that subspace, and at

$\lesssim 23.5$ days (CM19), thermally driven mass-loss models predict that planets will be rocky, whereas the gas-poor formation model predicts nonrocky planets. Therefore, populating this subspace with planets with known bulk compositions will inform the prevalence of each model as a function of host stellar mass.

Since the commencement of its prime mission in 2018 July, NASA’s Transiting Exoplanet Survey Satellite (TESS; Ricker et al. 2015) has uncovered a number of transiting planet candidates whose orbital periods and radii lie within the aforementioned subspace. These planets are valuable targets to conduct tests of competing radius valley emergence models across a range of stellar masses through the characterization of their bulk compositions using precise radial velocity (RV) measurements. Here we present the confirmation of one such planet from TESS: TOI-1235 b (TIC 103633434.01). Our analysis includes the mass measurement of TOI-1235 b from 38 RV observations from HARPS-N and HIRES. Our RV observations also reveal a second signal at 22 days that is suggestive of arising from stellar rotation, although some counterevidence favors a planetary interpretation that cannot be firmly ruled out by our data.

In Section 2 we present the properties of the host star TOI-1235. In Section 3 we present the TESS light curve and our suite of follow-up observations, including a measurement of the stellar rotation period from archival photometric monitoring. In Section 4 we present our data analysis and results. We conclude with a discussion and a summary of our results in Sections 5 and 6.

2. Stellar Characterization

TOI-1235 (TIC 103633434, TYC 4384-1735-1, Gaia DR2 1070387905514406400) is an early M dwarf located in the northern sky at a distance of 39.635 ± 0.047 pc⁴⁶ (Gaia Collaboration et al. 2018; Lindegren et al. 2018). The star has no known binary companions and is relatively isolated on the

⁴⁶ The Gaia DR2 parallax is corrected by $+0.08$ mas to account for the systematic offset reported by Stassun & Torres (2018).

Table 1
TOI-1235 Stellar Parameters

Parameter	Value	References
<i>TOI-1235, TIC 103633434, TYC 4384-1735-1,</i> Gaia DR2 1070387905514406400		
Astrometry		
R.A. (J2015.5), α	10:08:52.38	(1), (2)
Decl. (J2015.5), δ	+69:16:35.83	(1), (2)
R.A. proper motion, μ_α (mas yr ⁻¹)	196.63 \pm 0.04	(1), (2)
Decl. proper motion, μ_δ (mas yr ⁻¹)	17.37 \pm 0.05	(1), (2)
Parallax, ϖ (mas)	25.231 \pm 0.030	(1), (2)
Distance, d (pc)	39.635 \pm 0.047	(1), (2)
Photometry		
NUV _{GALEX}	20.58 \pm 0.10	(3)
u	15.55 \pm 0.30	(4)
$B_{\text{Tycho-2}}$	13.291 \pm 0.318	(5)
$V_{\text{Tycho-2}}$	11.703 \pm 0.103	(5)
V	11.495 \pm 0.056	(6)
G_{BP}	11.778 \pm 0.002	(1), (7)
G	10.8492 \pm 0.0005	(1), (7)
G_{RP}	9.927 \pm 0.001	(1), (7)
T	9.919 \pm 0.007	(8)
J	8.711 \pm 0.020	(9)
H	8.074 \pm 0.026	(9)
K_s	7.893 \pm 0.023	(9)
$W1$	7.81 \pm 0.03	(10)
$W2$	7.85 \pm 0.03	(10)
$W3$	7.77 \pm 0.30	(10)
$W4$	7.83 \pm 0.22	(10)
Stellar Parameters		
M_V	8.51 \pm 0.06	(11)
M_{K_s}	4.90 \pm 0.02	(11)
Effective temperature, T_{eff} (K)	3872 \pm 70	(11)
Surface gravity, $\log g$ (dex)	4.646 \pm 0.024	(11)
Metallicity, [Fe/H]	0.05 \pm 0.09	(11)
Stellar radius, R_s (R_\odot)	0.630 \pm 0.015	(11)
Stellar mass, M_s (M_\odot)	0.640 \pm 0.016	(11)
Stellar density, ρ_s (g cm ⁻³)	3.61 \pm 0.28	(11)
Stellar luminosity, L_s (L_\odot)	0.080 \pm 0.007	(11)
Projected rotation velocity, $v \sin i$ (km s ⁻¹)	<2.6	(11)
Rotation period, P_{rot} (days)	44.7 \pm 4.5	(11)

References. (1) Gaia Collaboration et al. 2018; (2) Lindegren et al. 2018; (3) Bianchi et al. 2017; (4) York et al. 2000; (5) Høg et al. 2000; (6) Reid et al. 2002; (7) Evans et al. 2018; (8) Stassun et al. 2019; (9) Cutri et al. 2003; (10) Cutri 2014; (11) this work.

sky, having just 21 faint sources within 2'5 resolved in Gaia Data Release 2 (DR2; Gaia Collaboration et al. 2018), all of which have $\Delta G > 6.5$. The astrometric, photometric, and physical stellar parameters are reported in Table 1.

We conducted an analysis of the star's broadband spectral energy distribution (SED) from the near-ultraviolet (NUV) to the mid-infrared (0.23–22 μm ; Figure 1). We constructed the SED following the procedures outlined in Stassun & Torres (2016) and Stassun et al. (2017, 2018a) using retrieved broadband NUV photometry from GALEX, the u -band magnitude from the Sloan Digital Sky Survey, Tycho-2 B - and V -band magnitudes, Gaia DR2 magnitudes, Two Micron All Sky Survey JHK_s near-IR magnitudes, and Wide-field Infrared Survey Explorer $W1$ – $W4$ IR magnitudes. Assuming zero extinction ($A_V = 0$), we fit the SED with a NextGen stellar

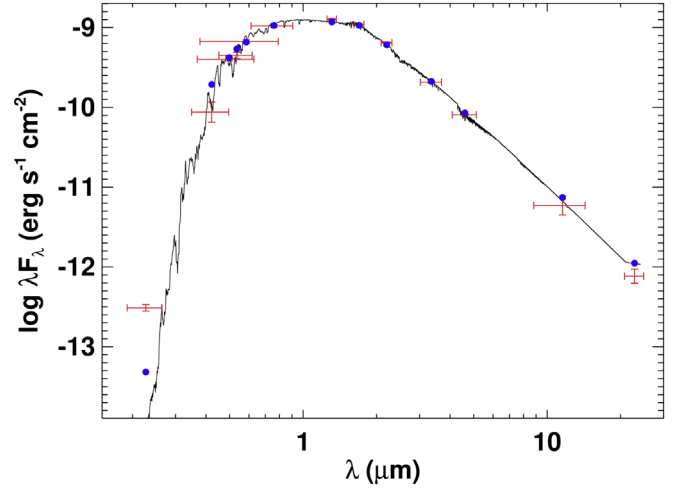


Figure 1. SED of TOI-1235. Red markers depict the photometric measurements, with horizontal error bars depicting the effective width of each passband. The black curve depicts the most likely stellar atmosphere model with $T_{\text{eff}} = 3950$ K. Blue circles depict the model fluxes over each passband.

atmosphere model (Hauschildt et al. 1999), treating the metallicity [Fe/H] and effective temperature T_{eff} as free parameters. We derive a weak constraint on [Fe/H] = -0.5 ± 0.5 (although we report the spectroscopically derived value in Table 1) and measure $T_{\text{eff}} = 3950 \pm 75$ K, which is consistent with T_{eff} derived from the HIRES spectra presented in Section 3.6.2 ($T_{\text{eff}} = 3872 \pm 70$ K). Integrating the SED at a distance of 39.6 pc gives a bolometric flux of $F_{\text{bol}} = (1.780 \pm 0.041) \times 10^{-9} \text{ erg s}^{-1} \text{ cm}^{-2}$, which corresponds to a stellar radius of $0.631 \pm 0.024 R_\odot$. As a consistency check, we also fit the SED with a Kurucz stellar atmosphere model (Kurucz 2013). Doing so, we recovered a bolometric flux and stellar radius that are consistent within 0.5σ of the values obtained when using the NextGen stellar models. The inferred stellar radius is also consistent with the value obtained from the empirically derived K_s -band radius–luminosity relation from Mann et al. (2015): $0.629 \pm 0.019 R_\odot$. In our study, we adopt the average of these two values: $R_s = 0.630 \pm 0.015 R_\odot$. Similarly, we derive the stellar mass using the K_s -band mass–luminosity relation from Benedict et al. (2016): $M_s = 0.640 \pm 0.016 M_\odot$.

In Section 3.2 we report our recovery $P_{\text{rot}} = 44.7$ days from archival MEarth photometry. This relatively long rotation period is consistent with the lack of rotational broadening observed in our high-resolution spectra presented in Section 3.6 ($v \sin i \leq 2.6 \text{ km s}^{-1}$) and the fact that H α is seen in absorption (Section 3.3). However, at face value, the GALEX NUV flux in Figure 1 appears to suggest a significant amount of chromospheric emission. This is at odds with the measured rotation period because, if real, the apparent excess NUV emission would imply a Rossby number of 0.2–0.3, or equivalently, $P_{\text{rot}} = 10$ –15 days (Wright et al. 2011; Stelzer et al. 2016). We note, however, that the NextGen atmosphere models do not self-consistently predict M dwarf UV emission from the chromosphere and transition region such that the apparent NUV excess from TOI-1235 is unlikely to be a true excess. The absence of chromospheric UV emission in the atmosphere models is noteworthy, as far-UV–NUV observations of M dwarfs have indicated that UV emission is widespread. In other words, even optically quiescent M dwarfs such as TOI-1235 are known to exhibit NUV spectra that are qualitatively similar

to those of more active M dwarfs that show chromospheric H α in emission (Walkowicz et al. 2008; France et al. 2013). Furthermore, the empirical GALEX NUV- K_s color relation with NUV flux from Ansdell et al. (2015), derived from the early M dwarf observations, reveals that $\log F_{\text{NUV}}/F_{\text{bol}} = -4.7 \pm 0.1$ for TOI-1235. This value is significantly less than $\log F_{\text{NUV}}/F_{\text{bol}} = -3.8 \pm 0.1$ based on the stellar atmosphere models used here. This discrepancy between observations of early M dwarfs and models supports the notion that the apparent NUV excess exhibited in Figure 1 is not a true NUV excess.

3. Observations

3.1. TESS Photometry

TOI-1235 was observed in three nonconsecutive TESS sectors between UT 2019 July 18 and 2020 February 18. TOI-1235 is a member of the Cool Dwarf target list (Muirhead et al. 2018) and was included in the TESS Input Catalog (TIC; Stassun et al. 2018b), the TESS Candidate Target List (CTL), and the Guest Investigator program 22198,⁴⁷ such that its light curve was sampled at 2-minute cadence. TESS observations occurred in CCD 3 on Camera 4 in sector 14 (UT 2019 July 18–August 14), in CCD 1 on Camera 2 in sector 20 (UT 2019 December 24–2020 January 20), and in CCD 2 on Camera 2 in sector 21 (UT 2020 January 21–February 18). Sector 14 was the first pointing of the spacecraft in the northern ecliptic hemisphere. As indicated in the data release notes,⁴⁸ to avoid significant contamination in cameras 1 and 2 due to scattered light by Earth and the Moon, the sector 14 field was pointed to $+85^\circ$ in ecliptic latitude, 31° north of its intended pointing from the nominal mission strategy. Despite this, all cameras in sector 14 continued to be affected by scattered light for longer periods of time compared to most other sectors owing to Earth’s position above the sunshade throughout the orbit. Camera 2 during sectors 20 and 21 was largely unaffected by scattered light except during data downloads and at the beginning of the second orbit in sector 21 owing to excess Moon glint.

The TESS images were processed by the NASA Ames Science Processing Operations Center (SPOC; Jenkins et al. 2016), which produce two light curves per sector called Simple Aperture Photometry (SAP) and Presearch Data Conditioning Simple Aperture Photometry (PDCSAP; Smith et al. 2012; Stumpe et al. 2012, 2014). The light curves are corrected for dilution during the SPOC processing, with TOI-1235 suffering only marginal contamination with a dilution correction factor of 0.9991. Throughout, we only consider reliable TESS measurements for which the measurement’s quality flag QUALITY is equal to zero. The PDCSAP light curve is constructed by detrending the SAP light curve using a linear combination of cotrending basis vectors (CBVs), which are derived from a principal component decomposition of the light curves on a per-sector, per-camera, per-CCD basis. TOI-1235’s PDCSAP light curve is depicted in Figure 2 and shows no compelling signs of coherent photometric variability from rotation. However, the set of CBVs (not shown) exhibits sufficient temporal structure that a linear combination of CBVs can effectively mask stellar rotation signatures greater than a few days. Thus, inferring P_{rot} for TOI-1235 from TESS would

be challenging and is addressed more effectively with ground-based photometric monitoring in Section 3.2.

Following light-curve construction, the SPOC conducts a subsequent transit search on each sector’s PDCSAP light curve using the Transiting Planet Search (TPS) module (Jenkins 2002; Jenkins et al. 2010). The TOI-1235.01 transit-like signal was detected in all three sectors independently and passed a set of internal data validation tests (Twicken et al. 2018; Li et al. 2019). The reported period of the planet candidate was 3.44 days in sectors 14 and 20 and three times that value (i.e., 10.33 days) in sector 21 owing to the low signal-to-noise ratio (S/N) of the individual transits. At 3.44 days, there are eight, six, and eight transits observed in each of the three sectors. The transit events are highlighted in Figure 2. The SPOC reported a preliminary transit depth of 841 ± 72 ppm, which corresponded to a planetary radius of $2.0 \pm 0.1 R_{\oplus}$ using our stellar radius (Table 1).

3.2. Photometric Monitoring with MEarth

Inactive early M dwarfs have typical rotation periods of 10–50 days (Newton et al. 2017). In Section 3.1 we described how measuring P_{rot} for TOI-1235 with TESS is intractable owing to the flexibility in the systematics model. Fortunately, MEarth-North has archival images of the field surrounding TOI-1235 that span 7.1 yr (UT 2008 October 2–2015 November 10), from which P_{rot} may be measured. MEarth-North is a telescope array located at the Fred Lawrence Whipple Observatory (FLWO) on Mount Hopkins, AZ. The facility consists of eight 40 cm telescopes, each equipped with a $25'6 \times 25'6$ field-of-view Apogee U42 camera, with a custom passband centered in the red optical (i.e., RG715). MEarth-North has been photometrically monitoring nearby mid- to late M dwarfs ($<0.33 R_{\odot}$) since 2008, in search of transiting planets (Berta et al. 2012; Irwin et al. 2015) and to conduct detailed studies of stellar variability (Newton et al. 2016). Although TOI-1235 was too large to be included in the initial target list (Nutzman & Charbonneau 2008), its position happens to be within $14'$ of an intentional target (GJ 1131) such that we are able to construct and analyze its light curve here for the first time.

To search for photometric signatures of rotation, we first retrieved the archival image sequence and computed the differential light curve of TOI-1235 as shown in Figure 3. We then investigated the Lomb–Scargle periodogram (LSP) of the light curve, which reveals a significant peak around 45 days that is not visible in the LSP of the window function (Figure 3). Using this value as an initial guess, we proceeded with fitting the light curve following the methods outlined in Irwin et al. (2006, 2011). The model includes systematics terms, predominantly from variations in the precipitable water vapor (PWV) column above the telescope, plus a sinusoidal term to model rotational modulation. As outlined in Newton et al. (2016), a “common mode” vector is constructed as a low-cadence comparison light curve that tracks variations in the PWV and is included in our systematics model as a linear term along with the FWHM of the MEarth point-spread function. With this full model, we measure $P_{\text{rot}} = 44.7 \pm 4.5$ days and a variability semiamplitude of 1.33 ppt. The detrended light curve, phase-folded to P_{rot} , is included in Figure 3. Figure 3 also reveals that the subtraction of our systematics plus rotation model from the light curve mitigates the 45-day signal in the LSP with no significant residual periodicities. The shallow

⁴⁷ PI: Courtney Dressing.

⁴⁸ https://archive.stsci.edu/tess/tess_drn.html

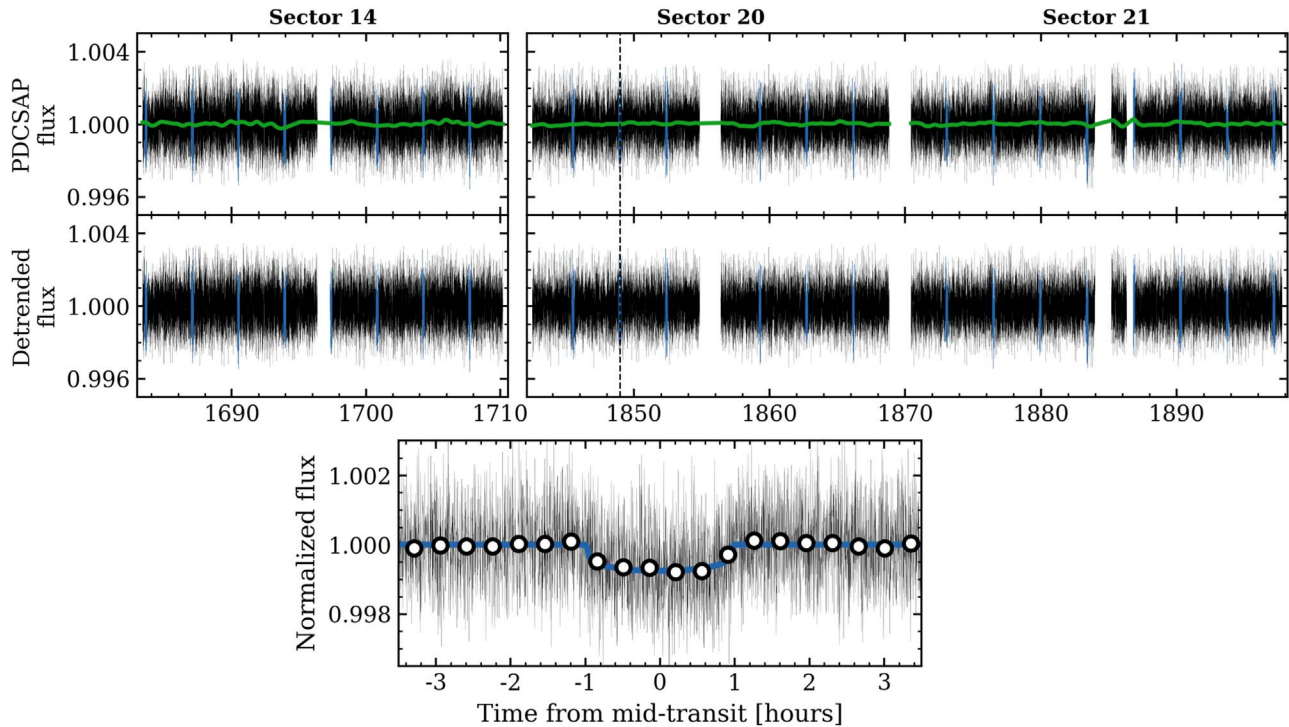


Figure 2. TESS light curve of TOI-1235 from sectors 14, 20, and 21. Top row: PDCSAP light curve following the removal of systematics via a linear combination of CBVs. The green curve depicts the mean GP model of residual temporally correlated noise (Section 4.1). The 3σ uncertainties on the mean GP model are smaller than the curve width. In-transit measurements are highlighted in blue throughout. The vertical dashed line highlights the epoch of the ground-based transit observation from LCOGT, which confirms the transit event on-target (Section 3.4). Middle row: detrended PDCSAP light curve. Bottom panel: phase-folded transit light curve of TOI-1235 b from 22 individual transit events. The maximum a posteriori transit model is depicted by the blue curve, while the white markers depict the binned photometry.

variability amplitude is unsurprising for relatively warm early M dwarfs like TOI-1235, whose spot-to-photosphere temperature contrasts are small (Newton et al. 2016). We note that knowledge of P_{rot} can be critical for the interpretation of RV signals, as even active regions with small temperature contrasts can induce large RV variations due to the suppression of convective blueshift (Dumusque et al. 2014).

3.3. Reconnaissance Spectroscopy with TRES

We began to pursue the confirmation of the planet candidate TOI-1235.01 by obtaining reconnaissance spectra with the Tillinghast Reflector Échelle Spectrograph (TRES) through coordination with the TESS Follow-up Observing Program (TFOP). TRES is a fiber-fed $R = 44,000$ optical échelle spectrograph (310–910 nm), mounted on the 1.5 m Tillinghast Reflector telescope at FLWO. Multiple spectra were obtained to search for RV variations indicative of a spectroscopic binary and to assess the level of surface rotation and chromospheric activity. We obtained two spectra at opposite quadrature phases of TOI-1235.01 on UT 2019 December 1 and 13 with exposure times of 2100 and 1200 s, which resulted in an S/N per resolution element of 31.4 and 26.0, respectively, at 519 nm in the order containing the information-rich Mg b lines.

The TRES RVs phase-folded to the TOI-1235.01 ephemeris are depicted in Figure 4 and show no significant variation, thus ruling out a spectroscopic binary. The cross-correlation function of the median spectrum with a rotating template of Barnard’s star is also shown in Figure 4 and reveals a single-lined spectrum with no significant rotational broadening ($v \sin i < 3.4 \text{ km s}^{-1}$). Lastly, the $H\alpha$ feature shown is seen in absorption, which is indicative of a chromospherically

inactive star and is consistent with $P_{\text{rot}} \gtrsim 10$ days (Newton et al. 2017). Taken together, our reconnaissance spectra maintain that TOI-1235.01 is a planetary candidate around a relatively inactive star.

3.4. Ground-based Transit Photometry with LCOGT

TESS’s large pixels ($21''$) can result in significant blending of target light curves with nearby sources. To confirm that the transit event occurs on-target, and to rule out nearby eclipsing binaries (EBs), we targeted a transit of TOI-1235.01 with seeing-limited photometric follow-up on UT 2019 December 31. This observation was scheduled after the planet candidate was detected in TESS sector 14 only and occurred during sector 20. The transit observation was scheduled using the TESS Transit Finder, a customized version of the *Tapir* software package (Jensen 2013). We obtained a z_s -band light curve from the McDonald Observatory with the 1 m telescope as part of the Las Cumbres Observatory Global Telescope network (LCOGT; Brown et al. 2013). The telescope is equipped with a 4096×4096 Sinistro camera whose pixel scale is 54 times finer than that of TESS: $0''.389 \text{ pixel}^{-1}$. We calibrated the full image sequence using the standard LCOGT BANZAI pipeline (McCully et al. 2018). The differential photometric light curve of TOI-1235, along with seven sources within $2.5'$, was derived from $7''$ uncontaminated apertures using the *AstroImageJ* software package (AIJ; Collins et al. 2017). The field was cleared of nearby EBs down to $\Delta z_s = 7.15$, as we did not detect eclipses from neighboring sources close to the expected transit time.

A full transit event was detected on-target and is included in Figure 4. We fit the light curve with a Mandel & Agol (2002)

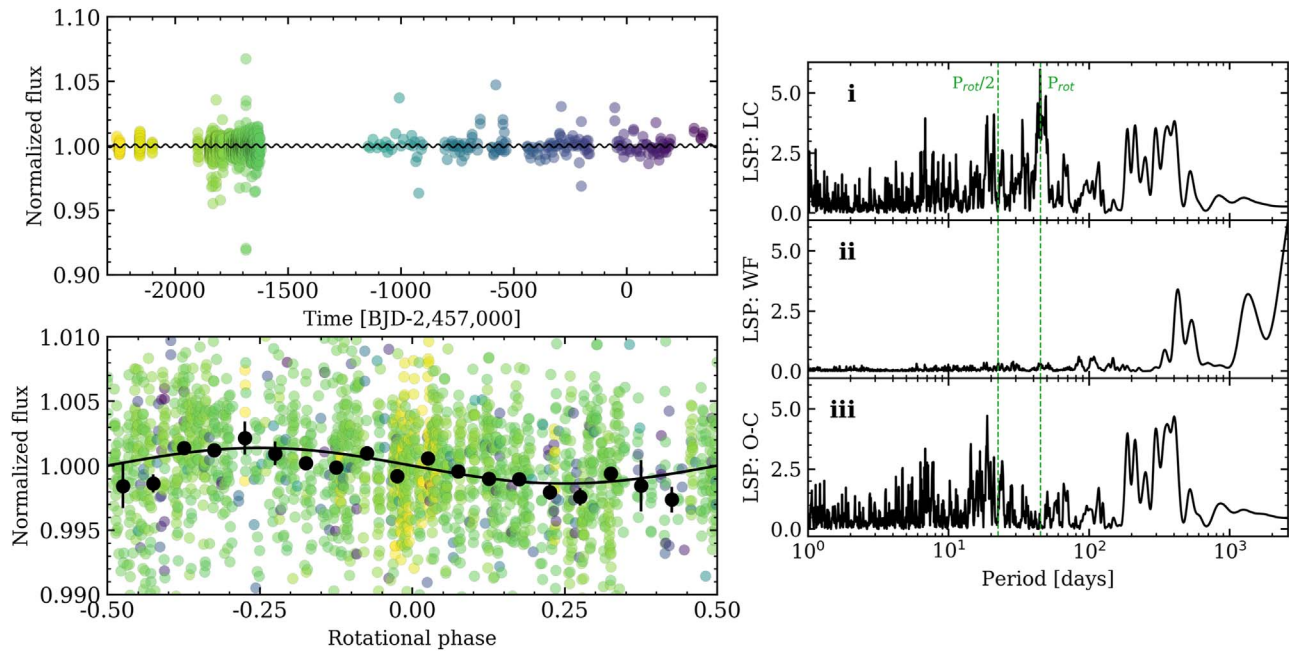


Figure 3. Measurement of the TOI-1235 photometric rotation period with MEarth-North. Top left panel: TOI-1235 differential light curve from archival MEarth-North photometry (2008 October–2015 November). Right panels: Lomb–Scargle periodograms of (i) the detrended light curve, (ii) the window function, and (iii) the photometric residuals after removal of the optimized sinusoidal fit with $P_{\text{rot}} = 44.7$ days. Bottom left panel: light curve phase-folded to P_{rot} . Black circles represent the binned light curve, while the solid black curve depicts the sinusoidal fit. The MEarth-North photometry is available as the Data behind the Figure.

(The data used to create this figure are available.)

transit model calculated using the *batman* software package (Kreidberg 2015). The shallow transit depth of TOI-1235.01 produces a low-S/N transit that does not provide strong constraints on most model parameters relative to what can be recovered from 22 transits in TESS. Consequently, we fix the model to a circular orbit with an orbital period, scaled semimajor axis, and impact parameter of $P = 3.44471$ days, $a/R_s = 13.2$, and $b = 0.45$, respectively. Furthermore, we set the quadratic limb-darkening parameters in the z_s band to $u_1 = 0.25$ and $u_2 = 0.33$ as interpolated from the Claret & Bloemen (2011) tables using the EXOFAST tool (Eastman et al. 2013). We fit the baseline flux, time of midtransit, and planet-to-star radius ratio via nonlinear least-squares optimization using the *scipy.curve_fit* function and find that $f_0 = 1.000$, $T_0 = 2,458,848.962$ BJD, and $r_p/R_s = 0.0295$. The transit is seen to arrive 63 minutes late relative to the linear ephemeris reported by the SPOC from sector 14 only. The transit depth of 0.867 ppt is 4.5 σ deeper than the TESS transit measured in our fiducial analysis (0.645 ppt; Section 4.1). Due to the similar wavelength coverage between the z_s and TESS passbands, and because of the large residual systematics often suffered by ground-based light curves of shallow transits, we attribute this discrepancy to unmodeled systematics rather than to a bona fide chromatic transit depth variation.

3.5. High-resolution Imaging

TESS’s large pixels also make the TESS light curves susceptible to contamination by very nearby sources that are not detected in Gaia DR2, nor in the seeing-limited image sequences. To clear the field of very nearby sources and a possible false positive in the form of a blended EB (Ciardi et al. 2015), we obtained two independent sets of high-resolution

follow-up imaging sequences as described in the following sections.

3.5.1. Adaptive Optics Imaging with Gemini/NIRI

We obtained adaptive optics (AO) images with *Gemini/NIRI* (Hodapp et al. 2003) on UT 2019 November 25 in the Br γ filter. We collected nine dithered images with integration times of 3.5 s. The data were reduced following a standard reduction procedure that includes bad pixel corrections, flat-fielding, sky subtraction, and image co-addition. The 5 σ contrast curve and the co-added image of TOI-1235 are included in the bottom right panel of Figure 4. These data provide sensitivity to visual companions with $\Delta\text{Br}\gamma \leq 5$ for separations >270 mas and $\Delta\text{Br}\gamma \leq 8.2$ beyond 1". We do not detect any visual companions within 5" of TOI-1235 within the 5 σ sensitivity of our observations.

3.5.2. Speckle Imaging with Gemini/Alopeke

We also obtained speckle interferometric images on UT 2020 February 16 using the ‘Alopeke instrument⁴⁹ mounted on the 8 m Gemini North telescope on the summit of Maunakea in Hawai‘i. ‘Alopeke simultaneously observes diffraction-limited images at 562 and 832 nm. Our data set consisted of 3 minutes of total integration time taken as sets of 1000×0.06 s images. Following Howell et al. (2011), we combined all images subjected to Fourier analysis to produce the speckle reconstructed imagery from which the 5 σ contrast curves are derived in each passband (bottom right panel of Figure 4). Our data reveal TOI-1235 to be a single star to contrast limits of

⁴⁹ <https://www.gemini.edu/sciops/instruments/alopeke-zorro/>

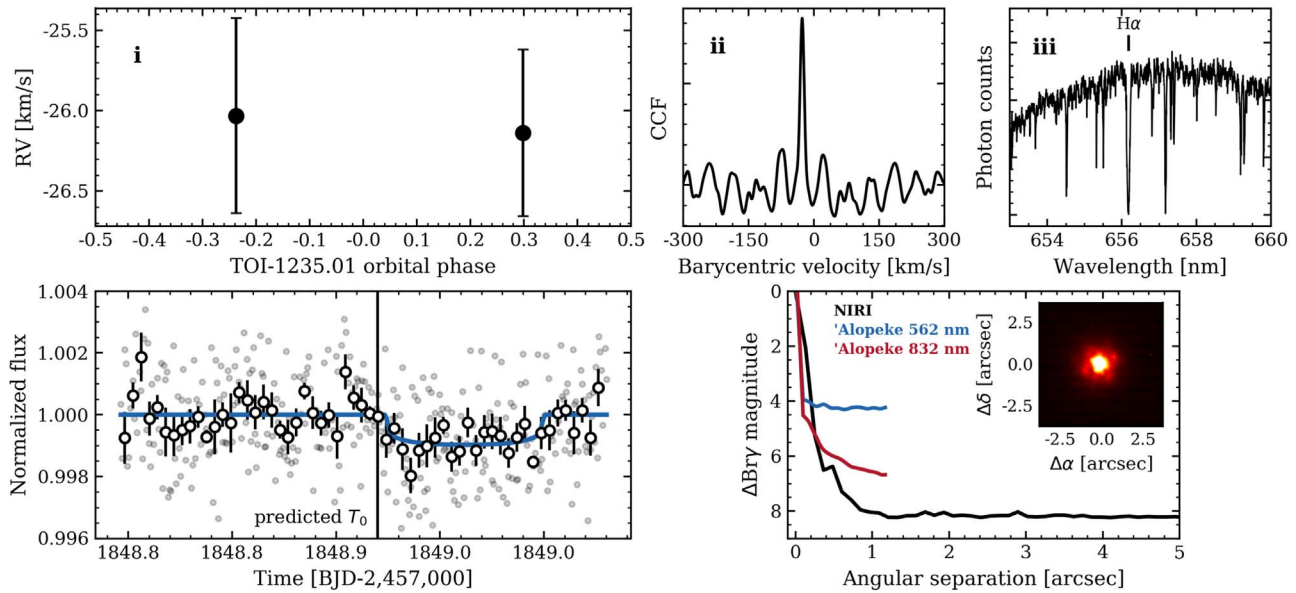


Figure 4. Summary of TFOF follow-up observations of TOI-1235 for planet validation purposes. Top row: results from TRES reconnaissance spectroscopy that (i) show no RV variations, thus ruling out a spectroscopic binary; (ii) reveal a single-lined CCF with no rotational broadening; and (iii) show H α in absorption. Bottom left panel: ground-based transit light curve obtained with LCOGT showing that the expected transit event occurred on-target and arrived 63 minutes late relative to the SPOC-reported linear ephemeris represented by the black vertical line. Open circles depict the light curve in 5.5-minute bins. The blue curve depicts the optimized transit fit to the LCOGT photometry. Bottom right panel: 5σ contrast curves from Gemini/NIRI AO-imaging (black), ‘Alopeke 562 nm’ speckle imaging (blue), and ‘Alopeke 832 nm’ speckle imaging (red). The inset depicts the co-added image from Gemini/NIRI AO-imaging centered on TOI-1235.

4.5–7 mag, eliminating essentially all main-sequence stars fainter than TOI-1235 within the spatial limits of 0.8–48 au.

Using our reconnaissance spectroscopy, ground-based transit follow-up, and high-resolution imaging observations as input (Figure 4), we used the *vespa* and *triceratops* statistical validation tools to compute the TOI-1235.01 false positive probability (FPP; Morton 2012; Giacalone & Dressing 2020). In both analyses we find that $\text{FPP} < 1\%$, and we will refer to the validated planet as TOI-1235 b for the remainder of this study.

3.6. Precise RVs

3.6.1. HARPS-N

We obtained 27 spectra of TOI-1235 with the HARPS-N optical échelle spectrograph at the 3.6 m Telescopio Nazionale Galileo on La Palma in the Canary Islands. The HARPS-N optical spectrograph, with a resolving power of $R = 115,000$, is stabilized in pressure and temperature, which enable it to achieve sub-meter-per-second accuracy under ideal observing conditions when sufficient S/N is attainable (Cosentino et al. 2012). The spectra were taken as part of the HARPS-N Collaboration Guaranteed Time Observations program between UT 2019 December 24 and 2020 March 12. The exposure time was set to 1800 s. In orders redward of order 18 (440–687 nm), we achieved a median S/N of 45.2 and a median measurement uncertainty of 1.22 m s^{-1} . TOI-1235 did not exhibit any rotational broadening in the HARPS-N spectra, leading to $v \sin i \leq 2.6 \text{ km s}^{-1}$, a result that is consistent with its measured rotation period $P_{\text{rot}} = 44.7 \pm 4.5$ days.

We extracted the HARPS-N RVs using the TERRA pipeline (Anglada-Escudé & Butler 2012). TERRA employs a template-matching scheme that is known to achieve improved RV measurement uncertainties on M dwarfs relative to the cross-correlation function (CCF) technique (Anglada-Escudé & Butler 2012). M dwarfs are particularly well suited to RV extraction via template matching because the line lists used to

define the binary mask for the CCF technique are incomplete and often produce a CCF template that is a poor match for cool M dwarfs. A master template spectrum is constructed by first shifting the individual spectra to the barycentric frame using the barycentric corrections calculated by the HARPS-N Data Reduction Software (DRS; Lovis & Pepe 2007), after masking portions of the wavelength-calibrated spectra wherein telluric absorption is $\geq 1\%$. A high-S/N template spectrum is then built by co-adding the individual spectra. TERRA then computes the RV of each spectrum relative to the template via least-squares matching the spectrum in velocity space. Throughout the extraction process, we only consider orders redward of order 18 such that the bluest orders at low S/N are ignored. The resulting RV time series is provided in Table 2.

3.6.2. HIRES

We obtained 11 additional spectra of TOI-1235 with the High Resolution Échelle Spectrometer on Keck I (HIRES; Vogt et al. 1994) as part of the TESS-Keck Survey (TKS) between UT 2019 December 10 and 2020 March 10. HIRES is an optical spectrograph at $R = 60,000$ that uses a heated iodine cell in front of the spectrometer entrance slit to perform its precise wavelength calibration between 500 and 620 nm. Against the forest of iodine cell features imprinted on the spectrum, we measure the relative Doppler shift of each spectrum while constraining the shape of the instrument profile at each epoch (Howard et al. 2010). The median exposure time was set to 900 s, which resulted in a median S/N at 550 nm of 124 and a median measurement uncertainty of 1.21 m s^{-1} , nearly identical to the median RV uncertainty in our HARPS-N time series. The HIRES RV measurements are also provided in Table 2.

We processed a single-epoch spectrum with an S/N of 96 pixel^{-1} using the *SpecMatch-Emp* algorithm (Yee et al. 2017) to independently derive spectroscopic stellar parameters.

Table 2
Radial Velocity Time Series of TOI-1235 from HARPS-N and HIRES

Time (BJD −2,457,000)	RV (m s ^{−1})	σ_{RV} (m s ^{−1})	Instrument
1890.653258	−0.119	0.975	HARPS-N
1905.851683	−7.358	1.281	HIRES
1906.724763	1.803	1.470	HARPS-N

(This table is available in its entirety in machine-readable form.)

The resulting effective temperature and metallicity are reported in Table 1. We also infer a stellar radius of $R_s = 0.61 \pm 0.10 R_\odot$, which is consistent with the values derived from our SED analysis and from the empirical M dwarf radius–luminosity relation.

4. Data Analysis and Results

Here we conduct a pair of independent analyses of our data to test the robustness of the recovered planetary parameters following the strategy adopted in Cloutier et al. (2020). In our fiducial analysis (Sections 4.1 and 4.2), we model the TESS light curve independently and use the resulting planet parameter posteriors as priors in our subsequent RV analysis. In Section 4.3 we conduct an alternative global analysis using the EXOFASTv2 software (Eastman et al. 2019).

4.1. TESS Transit Analysis

We begin our fiducial analysis by modeling the TESS PDCSAP light curve (Figure 2) in which the planet candidate TOI-1235.01 was originally detected. The PDCSAP light curve has already undergone systematics corrections via a linear combination of CBVs; however, some low-amplitude temporally correlated signals that are unrelated to planetary transits are seen to persist. We elect to model these signals as an untrained semiparametric Gaussian process (GP) simultaneously with the transit model of TOI-1235 b. We employ the *exoplanet* software package (Foreman-Mackey et al. 2019) to construct the GP and transit model in each step in our Markov Chain Monte Carlo (MCMC) simulation. Within *exoplanet*, analytical transit models are computed using the *STARRY* package (Luger et al. 2019), while *celerite* (Foreman-Mackey et al. 2017) is used to evaluate the marginalized likelihood of the GP model.

We adopt a covariance kernel of the form of a stochastically driven simple harmonic oscillator in Fourier space. The power spectral density of the kernel is

$$S(\omega) = \sqrt{\frac{2}{\pi}} \frac{S_0 \omega_0^4}{(\omega^2 - \omega_0^2)^2 + \omega_0^2 \omega^2 / Q^2}, \quad (1)$$

which is parameterized by the frequency of the undamped oscillator ω_0 ; the factor S_0 , which is proportional to the spectral power at ω_0 ; and the fixed quality factor $Q = \sqrt{0.5}$. We also include the baseline flux f_0 and an additive scalar jitter s_{TESS} in our noise model that we parameterize by $\{\ln \omega_0, \ln S_0 \omega_0^4, f_0, \ln s_{\text{TESS}}\}$. Our noise model is jointly fit with a transit model for TOI-1235 b with the following free parameters: the stellar mass M_s , stellar radius R_s , quadratic limb-darkening coefficients $\{u_1, u_2\}$, orbital period P , time of midtransit T_0 , planet radius r_p , impact parameter b , eccentricity e , and argument of periastron ω . Our full TESS model therefore contains 13 free parameters that are parameterized

Table 3
TESS Light Curve and RV Model Parameter Priors

Parameter	Fiducial Model Priors	EXOFASTv2 Model Priors
Stellar Parameters		
T_{eff} (K)	$\mathcal{N}(3872, 70)$	$\mathcal{N}(3872, 70)$
M_s (M_\odot)	$\mathcal{N}(0.640, 0.016)$	$\mathcal{N}(0.640, 0.016)$
R_s (R_\odot)	$\mathcal{N}(0.630, 0.015)$	$\mathcal{N}(0.630, 0.015)$
Light-curve Hyperparameters		
f_0	$\mathcal{N}(0, 10)$	$\mathcal{U}(-\text{inf}, \text{inf})$
$\ln \omega_0$ (day ^{−1})	$\mathcal{N}(0, 10)$...
$\ln S_0 \omega_0^4$	$\mathcal{N}(\text{Invar}(\mathbf{f}_{\text{TESS}}), 10)$...
$\ln s_{\text{TESS}}^2$	$\mathcal{N}(\text{Invar}(\mathbf{f}_{\text{TESS}}), 10)$...
u_1	$\mathcal{U}(0, 1)$	$\mathcal{U}(0, 1)$
u_2	$\mathcal{U}(0, 1)$	$\mathcal{U}(0, 1)$
Dilution	...	$\mathcal{N}(0, 0.1 \delta)^a$
RV Parameters		
$\ln \lambda$ (days)	$\mathcal{U}(\ln 1, \ln 1000)$...
$\ln \Gamma$	$\mathcal{U}(-3, 3)$...
P_{rot} (days)	$\mathcal{N}(46.1, 4.6)$...
$\ln a_{\text{HARPS-N}}$ (m s ^{−1})	$\mathcal{U}(-5, 5)$...
$\ln a_{\text{HIRES}}$ (m s ^{−1})	$\mathcal{U}(-5, 5)$...
$\ln s_{\text{HARPS-N}}$ (m s ^{−1})	$\mathcal{U}(-5, 5)$	$\mathcal{U}(-\text{inf}, \text{inf})$
$\ln s_{\text{HIRES}}$ (m s ^{−1})	$\mathcal{U}(-5, 5)$	$\mathcal{U}(-\text{inf}, \text{inf})$
$\gamma_{\text{HARPS-N}}$ (m s ^{−1})	$\mathcal{U}(-10, 10)$	$\mathcal{U}(-\text{inf}, \text{inf})$
γ_{HIRES} (m s ^{−1})	$\mathcal{U}(-10, 10)$	$\mathcal{U}(-\text{inf}, \text{inf})$
TOI-1235 b Parameters		
P (days)	$\mathcal{U}(-\text{inf}, \text{inf})^b$	$\mathcal{U}(-\text{inf}, \text{inf})$
T_0 (BJD −2,457,000)	$\mathcal{U}(-\text{inf}, \text{inf})^b$	$\mathcal{U}(-\text{inf}, \text{inf})$
$\ln r_p$ (R_\oplus)	$\mathcal{N}(0.5 \cdot \ln(Z) + \ln R_s, 1)^c$...
r_p/R_s	...	$\mathcal{U}(-\text{inf}, \text{inf})$
b	$\mathcal{U}(0, 1 + r_{p,b}/R_s)$...
$\ln K$ (m s ^{−1})	$\mathcal{U}(-5, 5)$...
K (m s ^{−1})	...	$\mathcal{U}(-\text{inf}, \text{inf})$
e	$\mathcal{B}(0.867, 3.03)^d$...
ω (rad)	$\mathcal{U}(-\pi, \pi)$...
$e \cos \omega$...	$\mathcal{U}(-1, 1)$
$e \sin \omega$...	$\mathcal{U}(-1, 1)$
$\sqrt{e} \cos \omega$	$\mathcal{U}(-1, 1) \dots$...
$\sqrt{e} \sin \omega$	$\mathcal{U}(-1, 1) \dots$...

Notes. Gaussian distributions are denoted by \mathcal{N} and are parameterized by mean and standard deviation values. Uniform distributions are denoted by \mathcal{U} and bounded by the specified lower and upper limits. Beta distributions are denoted by \mathcal{B} and are parameterized by the shape parameters α and β .

^a δ is the SPOC-derived dilution factor applied to the TESS light curve.

^b This prior in the fiducial model reflects that used in the TESS light analysis. However, its resulting posterior is used as an informative prior in the subsequent RV analysis.

^c The transit depth of TOI-1235.01 reported by the SPOC: $Z = 841$ ppm.

^d Kipping (2013).

by $\{f_0, \ln \omega_0, \ln S_0 \omega_0^4, \ln s_{\text{TESS}}^2, M_s, R_s, u_1, u_2, \ln P, T_0, \ln r_p, b, e, \omega\}$. Our adopted model parameter priors are listed in Table 3.

We execute an MCMC to sample the joint posterior probability density function (pdf) of our full set of model parameters using the *PyMC3* MCMC package (Salvatier et al. 2016) within *exoplanet*. The MCMC is initialized with four simultaneous chains, each with 4000 tuning steps and 3000 draws in the final sample. Point estimates of the maximum a posteriori (MAP) values from the marginalized posterior pdf's of the GP hyperparameters are selected to construct the

GP predictive distribution, whose mean function is treated as our detrending model of the PDCSAP light curve. This mean detrending function and the detrended light curve are both shown in Figure 2. Similarly, we recover the MAP point estimates of the transit model parameters to construct the transit model shown in the bottom panel of Figure 2. MAP values and uncertainty point estimates from the 16th and 84th percentiles for all model parameters are reported in Table 4.

4.2. Precise RV Analysis

We continue our fiducial analysis by jointly modeling the HARPS-N and HIRES RV time series. Here we are able to exploit the strong priors on P and T_0 derived from our analysis of the TESS light curve (Section 4.1).

The raw HARPS-N and HIRES RVs are shown in the top row of Figure 5, along with their Bayesian generalized Lomb–Scargle periodogram (BGLS; Mortier et al. 2015). The periodicity induced by TOI-1235 b is distinctly visible at 3.44 days. A preliminary RV analysis indicated that, following the removal of an optimized Keplerian solution for TOI-1235 b, the BGLS revealed a strong periodic signal at 22 days, which is seen at moderately low significance in the BGLS of the raw RVs in Figure 5. This periodicity is close to the first harmonic of the stellar rotation period at $P_{\text{rot}}/2 \approx 22.3$ days. As such, we interpret this signal as likely being produced by active regions on the rotating stellar surface. We note that this feature at $P_{\text{rot}}/2$ is similar to the first harmonic of P_{rot} observed on the Sun that has been shown to have either a comparable amount or at times more power than at P_{rot} (Mortier & Collier Cameron 2017; Milbourne et al. 2019). However, we note that simulated RV time series with injected quasi-periodic magnetic activity signals have been shown to produce spurious, and sometimes long-lived, periodogram signals that can masquerade as rotation signatures (Nava et al. 2020). But given that the 22-day signal is nearly identical to the first harmonic of the measured rotation period, we proceed with treating the 22-day signal as stellar activity and opt to simultaneously fit the HARPS-N and HIRES RVs with model components for TOI-1235 b, in the form of a Keplerian orbit, plus a quasi-periodic GP regression model of stellar activity whose covariance kernel as a function of time t takes the form

$$k_{ijs} = a_s^2 \left[-\frac{(t_i - t_j)^2}{2\lambda^2} - \Gamma^2 \sin^2 \left(\frac{2\pi|t_i - t_j|}{P_{\text{rot}}} \right) \right]. \quad (2)$$

The quasi-periodic kernel is parameterized by four hyperparameters: the covariance amplitude a_s , where s is the index over the two spectrographs; the exponential timescale λ ; the coherence Γ ; and the periodic timescale, which we initialize to $P_{\text{rot}}/2$ because of its apparent periodicity in the BGLS of the raw RVs. Because the temporally correlated signal that we are modeling with a GP likely originates from active regions on the rotating stellar surface, and given the fact that activity signals are inherently chromatic, we consider separate GP activity models for each spectrograph. We also maintain that the covariance hyperparameters $\{\lambda, \Gamma, P_{\text{rot}}\}$ are identical within each spectrograph’s GP activity model. We include an additive scalar jitter $s_{\text{RV},s}$ for each spectrograph to account for any excess noise in the activity model and fit for each spectrograph’s unique zero-point offset γ_s .

Table 4
Point Estimates of the TOI-1235 Model Parameters

Parameter	Fiducial Model Values ^a	EXOFASTv2Model Values ^b
TESS Light-curve Parameters		
Baseline flux, f_0	1.000024 ± 0.000010	1.000035 ± 0.000018
$\ln \omega_0$	1.45 ± 0.17	...
$\ln S_0 \omega_0^4$	$-0.16^{+0.52}_{-0.57}$...
$\ln s_{\text{TESS}}^2$	0.064 ± 0.006	...
TESS limb-darkening coefficient, u_1	$0.47^{+0.32}_{-0.24}$	$0.40^{+0.34}_{-0.26}$
TESS limb-darkening coefficient, u_2	$0.20^{+0.38}_{-0.35}$	$0.23^{+0.37}_{-0.38}$
Dilution	...	$0.09^{+0.21}_{-0.34}$
RV Parameters		
$\ln \lambda \text{ day}^{-1}$	$4.75^{+0.22}_{-0.10}$...
$\ln \Gamma$	$-0.04^{+1.9}_{-1.9}$...
$\ln P_{\text{rot}} \text{ day}^{-1}$	$3.82^{+0.10}_{-0.11}$...
$\ln a_{\text{HARPS-N}} \text{ m}^{-1} \text{ s}^{-1}$	$2.94^{+0.71}_{-0.69}$...
$\ln a_{\text{HIRES}} \text{ m}^{-1} \text{ s}^{-1}$	$1.46^{+0.76}_{-0.61}$...
Jitter, $s_{\text{HARPS-N}} \text{ (m s}^{-1}\text{)}$	$1.18^{+0.64}_{-0.75}$	$1.37^{+0.46}_{-0.40}$
Jitter, $s_{\text{HIRES}} \text{ (m s}^{-1}\text{)}$	$0.11^{+0.61}_{-0.09}$	$2.47^{+1.10}_{-0.83}$
Velocity offset, $\gamma_{\text{HARPS-N}} \text{ (m s}^{-1}\text{)}$	$-0.81^{+2.81}_{-3.03}$	$1.39^{+0.45}_{-0.43}$
Velocity offset, $\gamma_{\text{HIRES}} \text{ (m s}^{-1}\text{)}$	$0.69^{+2.50}_{-2.70}$	$-0.33^{+0.96}_{-0.99}$
TOI-1235 b Parameters		
Orbital period, P (days)	$3.444729^{+0.000031}_{-0.000028}$	$3.444727^{+0.000035}_{-0.000039}$
Time of midtransit, T_0 (BJD $-2,457,000$)	$1845.51696^{+0.000099}_{-0.000098}$	$1845.5173^{+0.0008}_{-0.0010}$
Transit duration D (hr)	$1.84^{+0.09}_{-0.16}$	$1.94^{+0.05}_{-0.04}$
Transit depth, Z (ppt)	$0.645^{+0.049}_{-0.044}$	$0.662^{+0.039}_{-0.038}$
Scaled semimajor axis, a/R_s	$13.20^{+0.41}_{-0.40}$	$13.15^{+0.34}_{-0.32}$
Planet-to-star radius ratio, r_p/R_s	0.0254 ± 0.0009	0.0257 ± 0.0007
Impact parameter, b	$0.45^{+0.21}_{-0.19}$	$0.33^{+0.15}_{-0.19}$
Inclination, i (deg)	$88.1^{+0.8}_{-0.9}$	$88.6^{+0.8}_{-0.6}$
$e \cos \omega$...	$0.00^{+0.03}_{-0.03}$
$e \sin \omega$...	$0.00^{+0.04}_{-0.06}$
$\sqrt{e} \cos \omega$	$0.07^{+0.13}_{-0.15}$...
$\sqrt{e} \sin \omega$	$-0.02^{+0.23}_{-0.23}$...
Eccentricity, e	$<0.15^c$	$<0.16^c$
Planet radius, $r_p \text{ (} R_{\oplus} \text{)}$	$1.738^{+0.087}_{-0.076}$	$1.763^{+0.071}_{-0.066}$
Log RV semi-amplitude, $\ln K \text{ m}^{-1} \text{ s}^{-1}$	$1.41^{+0.10}_{-0.13}$	$1.46^{+0.11}_{-0.13}$
RV semi-amplitude, $K \text{ (m s}^{-1}\text{)}$	$4.11^{+0.43}_{-0.50}$	$4.32^{+0.50}_{-0.51}$
Planet mass, $m_p \text{ (} M_{\oplus} \text{)}$	$6.91^{+0.75}_{-0.85}$	$7.53^{+0.88}_{-0.89}$
Bulk density, $\rho_p \text{ (g cm}^{-3}\text{)}$	$7.4^{+1.5}_{-1.3}$	$7.5^{+1.4}_{-1.2}$
Surface gravity, $g_p \text{ (m s}^{-2}\text{)}$	$22.6^{+3.5}_{-3.4}$	$23.7^{+3.3}_{-3.2}$
Escape velocity, $v_{\text{esc}} \text{ (km s}^{-1}\text{)}$	$22.4^{+1.3}_{-1.5}$	$23.1^{+1.2}_{-1.1}$
Semimajor axis, $a \text{ (au)}$	$0.03845^{+0.00037}_{-0.00040}$	$0.03846^{+0.00033}_{-0.00032}$
Insolation, $F \text{ (} F_{\oplus} \text{)}$	$53.6^{+5.3}_{-4.7}$	$53.6^{+4.2}_{-4.3}$
Equilibrium temperature, $T_{\text{eq}} \text{ (K)}$		
Bond albedo = 0.0	754 ± 18	754 ± 18
Bond albedo = 0.3	689 ± 16	689 ± 16
Keplerian Parameters of the 22-day RV Signal ^d		
Period (days)	...	$21.99^{+0.47}_{-0.32}$

Table 4
(Continued)

Parameter	Fiducial Model Values ^a	EXOFASTv2 Model Values ^b
Reference epoch (analogous to T_0) (BJD – 2,457,000)	...	$1835.34^{+0.89}_{-0.87}$
Log RV semi-amplitude, $\ln K$ m ⁻¹ s ⁻¹	...	$1.50^{+0.15}_{-0.14}$
RV semiamplitude, K (m s ⁻¹)	...	$4.50^{+0.62}_{-0.57}$
$e \cos \omega$...	$0.02^{+0.11}_{-0.09}$
$e \sin \omega$...	$0.09^{+0.18}_{-0.10}$

Notes.^a Our fiducial model features sequential modeling of the TESS light curve followed by the RV analysis conditioned on the results of the transit analysis.^b Our alternative analysis is a global model of the TESS and ground-based light curves, along with the RVs using the EXOFASTv2 software.^c 95% upper limit.^d The 22-day RV signal is modeled as an eccentric Keplerian in our EXOFASTv2 model, although we emphasize that here we do not attribute this signal to a second planet.

Our full RV model therefore consists of 14 free parameters: $\{\ln a_{\text{HARPS-N}}, \ln a_{\text{HIRES}}, \ln \lambda, \ln \Gamma, \ln P_{\text{rot}}, \ln s_{\text{RV,HARPS-N}}, \ln s_{\text{RV,HIRES}}, \gamma_{\text{HARPS-N}}, \gamma_{\text{HIRES}}, P, T_0, \ln K, h = \sqrt{e} \cos \omega, k = \sqrt{e} \sin \omega\}$, where K is the RV semiamplitude of TOI-1235 b. The adopted model parameter priors are included in Table 3. We fit the RV data with our full model using the affine-invariant ensemble MCMC sampler *emcee* (Foreman-Mackey et al. 2013), throughout which we use the *george* package (Ambikasaran et al. 2014) to evaluate the marginalized likelihood of the GP activity models. MAP point estimates of the model parameters are derived from their respective marginalized posterior pdf's and are reported in Table 4.

The second row in Figure 5 depicts the activity component in our RV model after the MAP Keplerian solution for TOI-1235 b is subtracted from the raw RVs. The residual periodicity close to $P_{\text{rot}}/2 = 22$ days becomes clearly visible in the BGLS of the RV activity signal. In our GP activity model, we measure an exponential timescale of $\lambda = 115 \pm 20$ days, indicating that active regions are relatively stable over a few rotation cycles. According to detailed investigations of periodogram signals in simulated RV time series, the persistence of the maximum RV activity peak at $P_{\text{rot}}/2$ is consistent with active region lifetimes on TOI-1235 exceeding P_{rot} (Nava et al. 2020).

In the third row of Figure 5, the BGLS of the TOI-1235 b signal is clearly dominated by the 3.44-day periodicity as expected. We measure an RV semiamplitude of $K = 4.11^{+0.43}_{-0.50}$ m s⁻¹, which is detected at 8.2σ and is clearly visible in the phase-folded RVs in Figure 5. The RV residuals, after removing each spectrograph's mean GP activity model and the MAP Keplerian solution, show no signs of any probable periodicities and have rms values of 1.90 and 1.65 m s⁻¹ for the HARPS-N and HIRES RVs, respectively. We note that these rms values exceed the typical RV measurement uncertainties of 1.2 m s⁻¹ and may be indicative of an incomplete RV model. We reserve an exploration of this prospect until Section 5.3.

4.3. A Global Transit and RV Analysis

To assess the robustness of the parameters derived from our fiducial modeling strategy (Sections 4.1 and 4.2), here we consider an alternative global model using the EXOFASTv2 exoplanet transit plus RV fitting package (Eastman et al. 2013, 2019).

Here we highlight a few notable differences between our fiducial analysis and the global model using EXOFASTv2. In our fiducial model of the TESS PDCSAP light curve, we simultaneously fit the data with a GP detrending model plus a transit model such that the uncertainties in the recovered planetary parameters are marginalized over our uncertainties in the detrending model. Conversely, EXOFASTv2 takes as input a pre-detrended light curve to which the transit model is fit. We construct the detrended light curve to supply to EXOFASTv2 using the mean function of the predictive GP distribution shown in Figure 2. With this method, the uncertainties in the planetary parameters of interest are not marginalized over uncertainties in the detrending model and may consequently be underestimated. Similarly, the RV model in our fiducial analysis considers temporally correlated RV activity signals and models them as a quasi-periodic GP. Conversely, modeling of the prominent 22-day signal in the RVs with EXOFAST requires one to assume a deterministic functional form for the signal in order to construct a more complete RV model. For this purpose, we model the 22-day signal as an eccentric Keplerian within EXOFASTv2. We adopt broad uniform priors on the signal's P and T_0 and adopt identical priors on its semiamplitude, $e \cos \omega$, $e \sin \omega$ as are used for TOI-1235 b (Table 3).

The EXOFASTv2 model has the important distinction of evaluating a global model that jointly considers the TESS photometry along with the HARPS-N and HIRES RVs. By virtue of this, the common planet parameters between these data sets (i.e., P , T_0 , e , ω) will be self-consistent. In particular, the eccentricity of TOI-1235 b will be jointly constrained by the transit duration, the RV solution, and the stellar density, which is constrained by our priors on the stellar mass and radius (Table 3). The EXOFASTv2 software also explicitly fits for any excess photometric dilution, therefore providing an improved accuracy on the transit depth and hence on the recovered planetary radius. Within EXOFASTv2, the dilution is defined as the fractional flux contribution from neighboring stars (see Section 12 Eastman et al. 2019).

We report the results from our global model in Table 4 and compare the planetary parameters to those derived from our fiducial analysis. All planetary parameters are consistent between our two analysis strategies at $<1\sigma$. In particular, in our fiducial and EXOFASTv2 analyses, we measure consistent values for the observables $r_p/R_s = 0.0254 \pm 0.0009$ and 0.0257 ± 0.0007 and $\ln K = 1.41^{+0.10}_{-0.13}$ and $1.46^{+0.11}_{-0.13}$. Given the identical stellar parameter priors in each analysis, this consistency directly translates into consistent measures of TOI-1235 b's fundamental planet parameters.

5. Discussion

5.1. Fundamental Planet Parameters

5.1.1. Orbital Separation, Mass, and Radius

Our analysis of the TESS PDCSAP light curve reveals that TOI-1235 b has an orbital period of $P = 3.444729^{+0.000031}_{-0.000028}$

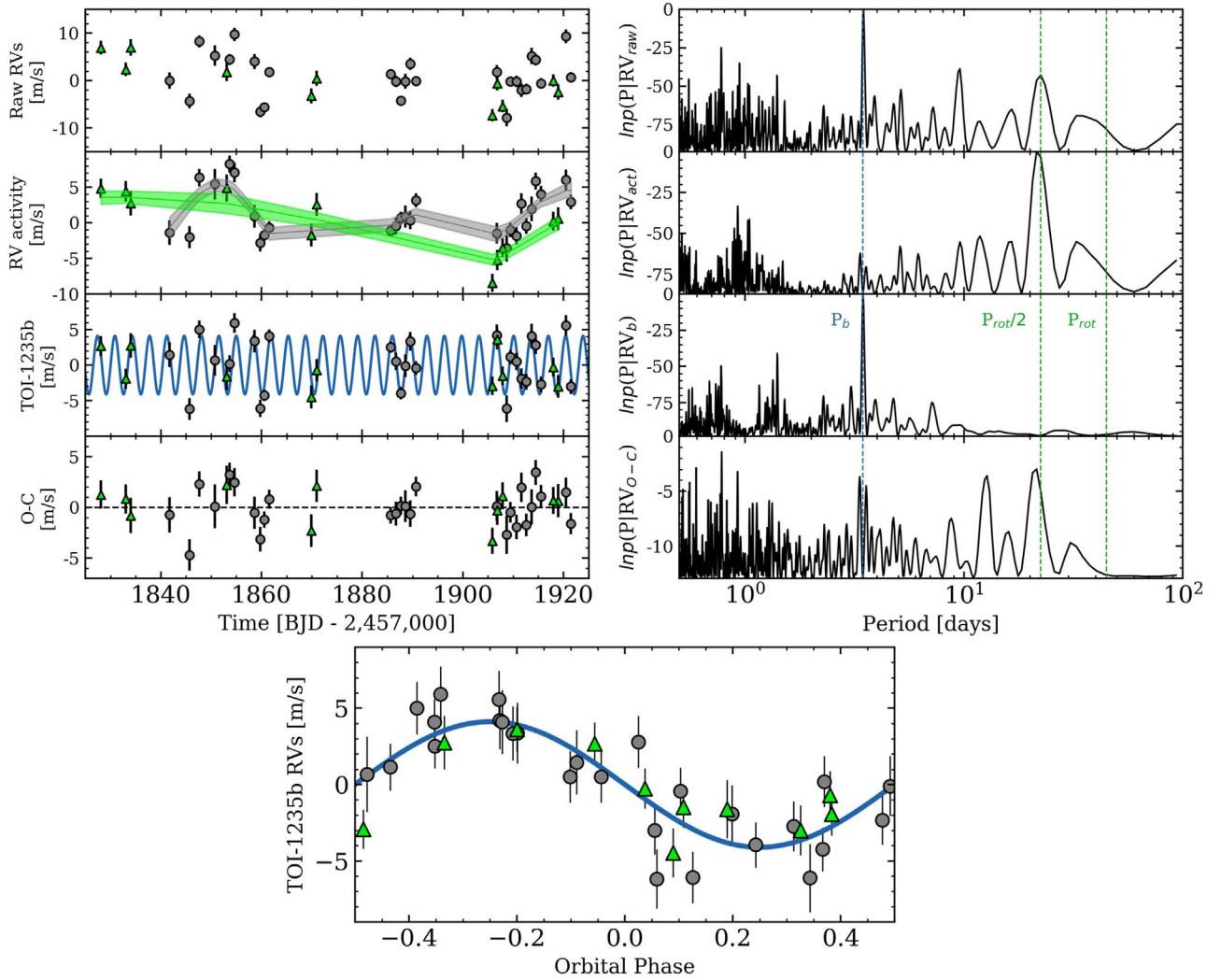


Figure 5. TOI-1235 RVs from HARPS-N (gray circles) and HIRES (green triangles). The data of each RV component and its corresponding model are depicted in the left column of the first four rows. Each component’s corresponding Bayesian generalized Lomb–Scargle periodogram is depicted in the adjacent right column, with the vertical dashed lines highlighting the orbital period of TOI-1235 b ($P = 3.44$ days), the stellar rotation period ($P_{\text{rot}} = 44.7$ days), and its first harmonic ($P_{\text{rot}}/2 = 22.3$ days). First row: raw RVs. Second row: RV activity at $P_{\text{rot}}/2$ modeled as separate quasi-periodic GPs for each spectrograph. Third row: Keplerian orbital solution for TOI-1235 b. Fourth row: RV residuals. Bottom panel: phase-folded RV signal from TOI-1235 b.

days and a planetary radius of $r_p = 1.738^{+0.087}_{-0.076} R_{\oplus}$. The corresponding semimajor axis for TOI-1235 b is $a = 0.03845^{+0.00037}_{-0.00040}$ au, where it receives $53.6^{+5.3}_{-4.7}$ times Earth’s insolation. Assuming uniform heat redistribution and a Bond albedo of zero, TOI-1235 b has an equilibrium temperature of $T_{\text{eq}} = 754 \pm 18$ K.

From our RV analysis, we obtain an 8.1σ planetary mass measurement of $m_p = 6.91^{+0.75}_{-0.85} M_{\oplus}$. Taken together, the mass and radius of TOI-1235 b give a bulk density of $\rho_p = 7.4^{+1.5}_{-1.3} \text{ g cm}^{-3}$. In Figure 6 we add TOI-1235 b to the mass–radius diagram of small M-dwarf planets with $\geq 3\sigma$ mass measurements. Comparing TOI-1235 b’s mass and radius to internal structure models of two-layer, fully differentiated planet interiors (Zeng & Sasselov 2013) reveals that the bulk composition of TOI-1235 b is consistent with an Earth-like composition of 33% iron plus 67% silicate rock by mass.

Intriguingly, the mass and radius of TOI-1235 b are nearly identical to those of LHS 1140 b, despite LHS 1140 b having a wider 25-day orbit around a mid-M dwarf, thus making it much more temperate than TOI-1235 b ($T_{\text{eq}} = 230$ K; Dittmann et al. 2017; Ment et al. 2019). Both planets are situated within the

radius valley around low-mass stars (CM19) and have masses that appear to represent the upper limit of terrestrial planet masses in a planetary mass regime where rocky Earth-like planets are inherently rare (i.e., 5–10 M_{\oplus} ; Figure 6). These planets offer unique opportunities to study nature’s largest terrestrial planets, whose tectonic and outgassing processes may differ significantly from those on Earth-sized terrestrial planets (Valencia et al. 2007).

With the planetary mass measurement presented herein, TOI-1235 adds to the growing list of small planets transiting M dwarfs with precise RV masses (GJ 3470, Bonfils et al. 2012; GJ 1214, Charbonneau et al. 2009; GJ 1132, Bonfils et al. 2018; K2-3, Damasso et al. 2018; K2-18, Cloutier et al. 2019b; LHS 1140, Ment et al. 2019), which has been rapidly expanding since the launch of TESS (GJ 357, Luque et al. 2019; GJ 1252, Shporer et al. 2020; L98-59, Cloutier et al. 2019a; L168-9, Astudillo-Defru et al. 2020; LTT 3780, Cloutier et al. 2020; Nowak et al. 2020). Notably, TOI-1235 b also directly contributes to the completion of the TESS level-one science requirement of obtaining precise masses for 50 planets smaller than four Earth radii.

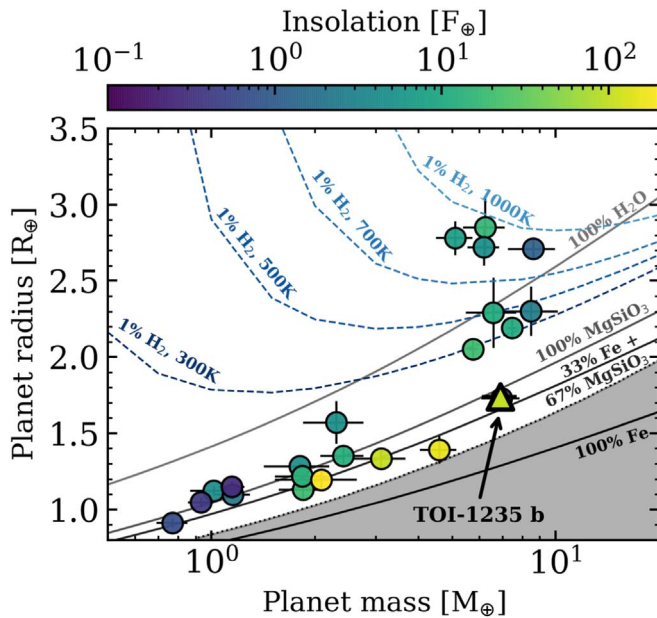


Figure 6. Mass–radius diagram for small planets orbiting M dwarfs, including TOI-1235 b (triangle). Error bars on the TOI-1235 b mass and radius are smaller than the marker, which lies directly on top of LHS 1140 b in this space. The solid curves depict internal structure models with mass fractions of 100% water, 100% silicate rock, 33% iron plus 67% rock (i.e., Earth-like), and 100% iron (Zeng & Sasselov 2013). The dashed curves depict models of Earth-like cores hosting H_2 envelopes with 1% envelope mass fractions at various equilibrium temperatures (Zeng et al. 2019). The shaded region bounded by the dotted curve highlights the forbidden region according to models of maximum collisional mantle stripping by giant impacts (Marcus et al. 2010).

5.1.2. Iron and Envelope Mass Fractions

We wish to place self-consistent limits on the iron mass fraction X_{Fe} and envelope mass fraction X_{env} of TOI-1235 b. Here the iron mass fraction is defined as the ratio of the total mass of the core and mantle that is composed of iron, with the remainder in magnesium silicate. The envelope mass fraction is then defined as the fraction of the planet’s total mass that is in its gaseous envelope. However, it is important to note that these values are degenerate such that we cannot derive a unique solution given only the planet’s mass and radius. For example, the bulk composition of TOI-1235 b is consistent with being Earth-like, thus suggesting a small envelope mass fraction,⁵⁰ but one could also imagine a more exotic scenario that is consistent with the planet’s mass and radius of a planetary core with $X_{\text{Fe}} = 1$, surrounded by an extended H/He envelope. In the simplest case, we assume that magnesium silicate and iron are the only major constituents of TOI-1235 b’s bulk composition such that $X_{\text{env}} = 0$. Under this assumption, we derive X_{Fe} by Monte Carlo sampling the uncorrelated marginalized posterior pdf’s of m_p and r_p and use the analytical rock/iron mass–radius relation from Fortney et al. (2007) to recover X_{Fe} . We find that TOI-1235 b has an iron mass fraction of $X_{\text{Fe}} = 20^{+15}_{-12}\%$ that is $<46\%$ at 90% confidence.

To infer the distribution of envelope mass fractions that are consistent with the data, we first impose a physically motivated prior on X_{Fe} of $\mathcal{N}(0.33, 0.10)$. The relatively narrow width of this Gaussian prior is qualitatively supported by observations of nearby Sun-like stellar metallicities that show that the abundance ratios of Mg/Fe, Si/Fe, and Mg/Si at similar ages

and metallicities vary by less than 10%. This indicates a low level of compositional diversity in the refractory building blocks of planets (Bedell et al. 2018). The width of our X_{Fe} Gaussian prior is chosen in an ad hoc way to approximately reflect this level of chemical diversity. The homogeneity of refractory chemical abundances among Sun-like stars, coupled with their similar condensation temperatures (Lodders 2003), suggests a narrow range in iron mass fractions among close-in terrestrial planets. This assertion is supported by the locus of terrestrial planets with $r_p \lesssim 1.8 R_{\oplus}$ that are consistent with an Earth-like bulk composition (Figure 6). This concept of similar X_{Fe} values is particularly compelling for the most massive terrestrial planets (e.g., TOI-1235 b), for which a significant increase in X_{Fe} by collisional mantle stripping is energetically infeasible owing to the large binding energies of such planets (Marcus et al. 2010).

To proceed with deriving the distribution of TOI-1235 b envelope mass fractions assuming an Earth-like core, we extend the solid two-layer interior structure model to include an H/He envelope with a mean molecular weight equal to that of a solar-metallicity gas ($\mu = 2.35$). Our adopted planetary model is commonly used for sub-Neptune-sized planets (e.g., Rafikov 2006; Lee & Chiang 2015; Ginzburg et al. 2016; Owen & Wu 2017; Gupta & Schlichting 2019). This model features a solid core surrounded by an H/He gaseous envelope that, depending on the planetary parameters, either is fully radiative throughout or may be convective in the deep interior up to the height of the radiative–convective boundary (RCB), above which the atmosphere becomes radiative and isothermal with temperature T_{eq} . The latter scenario represents the general case, whereas the former is only invoked when the planetary parameters result in a height of the RCB that is less than the atmospheric pressure scale height at T_{eq} . To first order, the height of the RCB above the planetary surface r_{RCB} , and hence X_{env} , is determined by $\{T_{\text{eq}}, m_p, r_p, X_{\text{Fe}}\}$. Each of T_{eq} , m_p , and r_p are directly constrained by our data if we assume a Bond albedo to infer T_{eq} . We derive r_{RCB} and X_{env} by Monte Carlo sampling X_{Fe} from its prior, along with the zero-albedo T_{eq} , m_p , and r_p from their respective marginalized posterior pdf’s. We then rescale each T_{eq} draw by $(1 - A_B)^{1/4}$, where A_B is the Bond albedo. Super-Earth bond albedos have poor empirical constraints, so we opt to condition a broad uniform prior on A_B of $\mathcal{U}(0.1, 0.8)$ based on the solar system planets. Lastly, although we expect r_{RCB} to shrink over time as the H/He envelope cools and contracts, this effect on X_{env} is known to be a weak function of planet age (Owen & Wu 2017) such that we fix the age of TOI-1235 to 5 Gyr in our calculations.

We use a customized version of the *EvapMass* software (Owen & Campos Estrada 2020) to self-consistently solve for r_{RCB} and X_{env} given samples of $\{T_{\text{eq}}, m_p, r_p, X_{\text{Fe}}\}$. We attempt to sample these parameters in 10^5 realizations, although not all parameter combinations are physically capable of producing a self-consistent solution. In practice, our Monte Carlo sampling results in 94,131 successful planetary model realizations (i.e., 94.1% success rate). The resulting distributions of X_{Fe} and X_{env} that are consistent with our measurements of TOI-1235 b are shown in Figure 7. We find that 41.1% of successful planet model realizations have fully radiative atmospheres, with the remaining 58.9% being convective in the lower atmosphere. These models produce largely disparate results with radiative atmospheres being favored for increasingly smaller X_{Fe} and always having $X_{\text{env}} \lesssim 10^{-3}$. Conversely, atmospheres with a

⁵⁰ Earth has an envelope mass fraction of $<10^{-6}$.

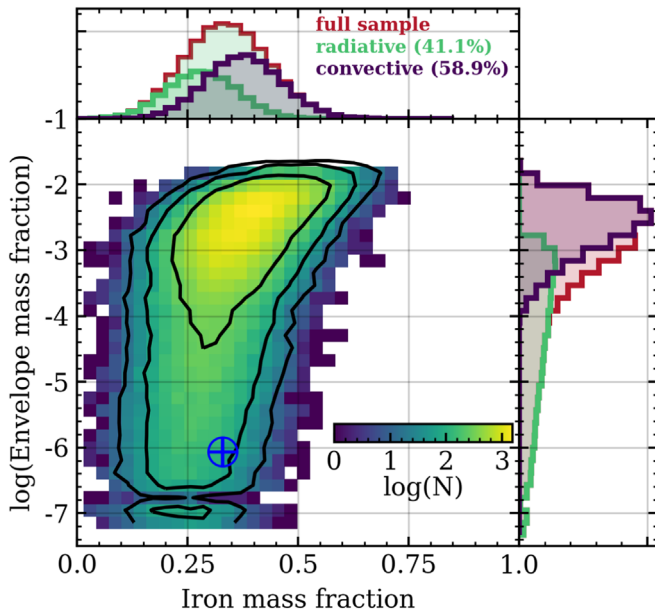


Figure 7. Joint distribution of TOI-1235 b’s iron mass and envelope mass fractions to be consistent with its measured mass and radius. The color map represents the number of successful planet models given X_{env} and X_{Fe} , while the contours highlight the 68th, 95th, and 99th percentiles. The top and right 1D histograms depict the marginalized distributions of X_{Fe} and $\log_{10}(X_{\text{env}})$, respectively, for the full sample (red), plus the subset of realizations with radiative atmospheres (green) and convective atmospheres (blue). The blue plus sign highlights Earth.

deep convective region are more extended, thus requiring a more compressed core (i.e., large X_{Fe}) and larger X_{env} . Overall we see the positive correlation between X_{Fe} and X_{env} because at a fixed m_p the core radius must shrink with increasing X_{Fe} , which requires the envelope to become extended to match the observed radius. Extending the envelope increases the limits of integration over the atmospheric density profile from the planetary surface to the top of the atmosphere, consequently increasing the envelope mass. With our models, we find that TOI-1235 b has a maximum envelope mass fraction of 2.3%. Marginalizing over all other model parameters and both atmospheric equations of state, we find that X_{env} must be $<0.5\%$ at 90% confidence.

5.2. Implications for the Origin of the Radius Valley around Mid-M Dwarfs

Observational studies of the occurrence rate of close-in planets around Sun-like stars have revealed a bimodality in the distribution of planetary radii known as the radius valley (e.g., Fulton et al. 2017; Fulton & Petigura 2018; Mayo et al. 2018). This dearth of planets between 1.7 and $2.0 R_{\oplus}$ around Sun-like stars likely marks the transition between rocky planets and larger planets that host extended gaseous envelopes. Physical models of the emergence of the radius valley from thermally driven atmospheric mass loss (i.e., photoevaporation or core-powered mass loss), and from terrestrial planet formation in a gas-poor environment, make distinct predictions regarding the slope of the radius valley in period–radius space. The slope of the radius valley around Sun-like stars with $T_{\text{eff}} > 4700$ K was measured by Martinez et al. (2019) using the stellar sample from Fulton et al. (2017). The recovered slope was shown to be consistent with model predictions from thermally driven

atmospheric mass loss ($r_{p,\text{valley}} \propto P^{-0.15}$; Lopez & Rice 2018). On the other hand, the slope around lower-mass dwarfs with $T_{\text{eff}} < 4700$ K (i.e., mid-K to mid-M dwarfs) was measured by CM19 and was shown to have a flipped sign that instead was consistent with predictions from gas-poor formation ($r_{p,\text{valley}} \propto P^{0.11}$; Lopez & Rice 2018). One interpretation of this is that the dominant mechanism for sculpting the radius valley is stellar mass dependent and that thermally driven mass loss becomes less efficient toward mid- to late M dwarfs, where a new formation pathway of terrestrial planets in a gas-poor environment emerges (CM19). The stellar mass at which this proposed transition occurs is not well resolved by occurrence rate measurements, but it may be addressed by the detailed characterization of individual planets that span the model predictions in period–radius space (e.g., TOI-1235 b).

Differences in the slopes of the radius valley around Sun-like and lower-mass stars naturally carve out a subset of the period–radius space in which the models make opposing predictions for the bulk compositions of planets. This subspace around low-mass stars cooler than 4700 K was quantified by CM19 and is highlighted in Figure 8. At periods less than 23.5 days, planets within the highlighted subspace are expected to be rocky according to models of thermally driven hydrodynamic escape. Conversely, gas-poor formation models predict that those planets should instead be nonrocky with envelope mass fractions of at least a few percent depending on their composition. TOI-1235 b falls within this region of interest and therefore provides direct constraints on the efficiency of the competing physical processes on close-in planets around early M dwarfs.

Our transit and RV analyses revealed that TOI-1235 b is a predominantly rocky planet with an iron mass fraction of $20^{+15}_{-12}\%$ and an envelope mass fraction that is $<0.5\%$ at 90% confidence. Given its period and radius, this finding is consistent with models of thermally driven mass loss but is inconsistent with the gas-poor formation scenario. Indeed, based on the photoevaporation-driven hydrodynamic escape simulations by Lopez & Fortney (2013), the mass of TOI-1235 b places its insolation flux ($F = 53.6^{+5.3}_{-4.7} F_{\oplus}$) right at the threshold insolation required for the planet to lose its gaseous envelope: $F_{\text{threshold}} = 52 \pm 14 F_{\oplus}$.⁵¹ These results suggest that thermally driven mass loss continues to be an efficient process for sculpting the radius valley around early M dwarfs like TOI-1235. CM19 suggested that although thermally driven mass loss seems to be prevalent around Sun-like stars, evolution in the structure of the radius valley with stellar mass suggests that this prevalence weakens with decreasing stellar mass and that gas-poor formation may emerge as the dominant mechanism for sculpting the radius valley around early to mid-M dwarfs. Although the stellar mass at which this proposed transition occurs has yet to be resolved, the rocky nature of TOI-1235 b further suggests that the stellar mass at which this transition occurs is likely less than that of TOI-1235 ($0.640 \pm 0.016 M_{\odot}$).

As an aside, we note that distinguishing between photoevaporation and core-powered mass loss cannot be achieved with the data presented herein. Fortunately, the distinction can be addressed at the planet population level by investigating the radius valley’s dependence with time and with stellar mass (Gupta & Schlichting 2020).

⁵¹ Assuming a fixed mass-loss efficiency of 10% (Lopez et al. 2012).

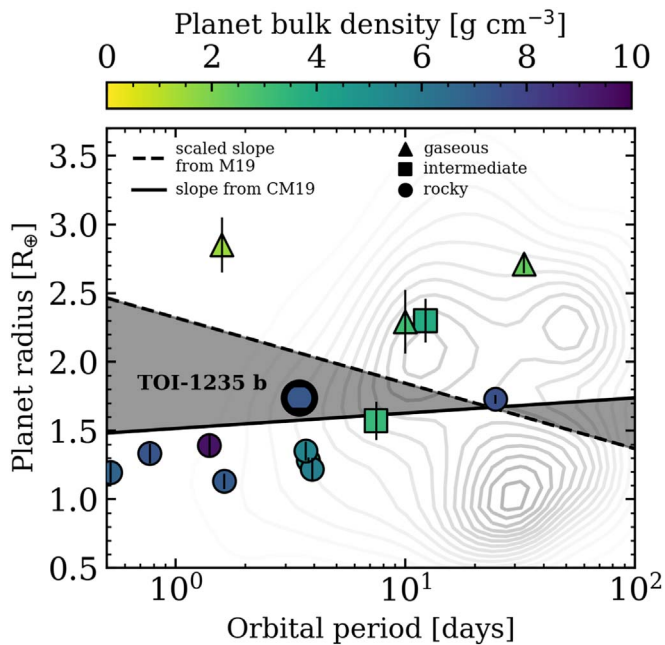


Figure 8. Period–radius diagram for small planets orbiting M dwarfs with precise RV masses, including TOI-1235 b (thick circle). The dashed and solid lines depict the locations of the radius valley around low-mass stars from model predictions of thermally driven atmospheric mass loss and from gas-poor terrestrial planet formation, respectively. The shaded regions highlight where the predictions of planetary bulk compositions are discrepant between the two models. Contours represent the planetary occurrence rates around low-mass stars (CM19). Planet marker shapes depict the planet’s compositional disposition as either rocky (circles), gaseous (triangles), or intermediate (squares). Marker colors indicate the planet’s bulk density.

5.3. Testing the Prospect of a Second Planet around TOI-1235

Recall that after removing the TOI-1235 b signal from our RV time series, a strong residual periodicity emerges at about 22 days (second row in Figure 5). We initially interpreted this signal as being likely related to rotationally induced stellar activity because of its proximity to the first harmonic of the probable stellar rotation period inferred from ground-based photometric monitoring ($P_{\text{rot}} = 44.7 \pm 4.5$ days; Figure 3). Although the measurement of P_{rot} makes the 22-day RV signal suggestive of being related to stellar activity, here we conduct a suite of tests that instead favor a planetary origin.

The treatment of the 22-day RV signal as either a quasi-periodic GP in our fiducial model or an eccentric Keplerian in our EXOFASTv2 global model (see Sections 4.2 and 4.3) gives an activity semiamplitude of $\approx 5 \text{ m s}^{-1}$. This value appears to be at odds with reasonable predictions of the RV signal based on the star’s long-term photometric variability from ground-based monitoring (Section 3.2). Using the FF' model to predict the activity-induced RV variations from photometric variability (Aigrain et al. 2012), we would expect the semiamplitude of the TOI-1235 RV activity signal to be at the level of $1\text{--}2 \text{ m s}^{-1}$ instead of the observed value of 5 m s^{-1} under the single-planet model. However, it is important to note that photometry is not a perfect predictor of RV variations because (i) stellar activity undergoes cycles and there is no guarantee that the level of activity is constant between the epochs of photometric monitoring and the RV observations, (ii) photometry is not sensitive to all spot distributions (Aigrain et al. 2012), and (iii) bright chromospheric plages can produce RV variations with amplitudes similar to those induced by spots of the same size,

but with potentially 10 times less flux variations (Dumusque et al. 2014). Therefore, the discrepancy between the observed RV activity variations and the FF' model predictions is merely suggestive that our RV activity models are overpredicting the amplitude of the RV activity signal, which would then require an additional RV component to model the excess signal in the RV residuals.

Rotationally induced RV signals from active regions arise from the temperature difference between the active regions and the surrounding stellar surface. As such, the active region contrast has an inherent wavelength dependence that increases toward shorter wavelengths such that RV activity signals should be larger at bluer wavelengths (Reiners et al. 2010). We elected to investigate the chromatic dependence of the 22-day RV signal by considering sets of “blue” and “red” RVs from HARPS-N. We rederived the HARPS-N RVs using the same methodology as in our fiducial analysis but focused separately on the spectral orders 0–45 (388–550 nm) and 46–68 (550–689 nm) to derive sets of blue and red RVs, respectively. Each range of orders was selected to achieve a comparable median RV measurement uncertainty in each time series of 1.98 and 2.04 m s^{-1} . We then investigated the chromatic dependence of the probability of the 3.44- and 22-day periodicities in the BGLS. While the 22-day signal was marginally more probable in the red RVs, we found that the planetary signal varied by many more orders of magnitude than the 22-day signal. This behavior is unexpected for a planetary signal that is known to be achromatic. We therefore concluded that this chromatic analysis of our data set is unreliable, and we make no claims regarding the physical origin of the 22-day signal based on its chromatic dependence.

To explicitly test the idea that an additional RV component is required to completely model the data, we considered a two-planet RV model with components for TOI-1235 b, a second Keplerian “c” at 22 days, plus quasi-periodic GP activity models for each spectrograph with an imposed prior on its periodic timescale equal to that of P_{rot} : $\mathcal{N}(44.7, 4.5)$ days. We sampled the two-planet model parameter posteriors using an identical method to what was used in our fiducial analysis of the one-planet RV model (Section 4.2). We adopted narrow uniform priors on P_c of $\mathcal{U}(17, 27)$ days and on $T_{0,c}$ of $\mathcal{U}(1821.5, 1848.5)$ BJD $- 2,457,000$. The resulting Keplerian model parameters on the hypothetical planet “c” are reported in Table 5. We find that the hypothetical planet would have a period of $P_c = 21.8^{+0.9}_{-0.8}$ days and an RV semiamplitude of $K_c = 4.2^{+1.2}_{-1.7}$, which implies a minimum mass of $m_{p,c} \sin i = 13.0^{+3.8}_{-5.3} M_{\oplus}$.

We now have one- and two-planet RV models of the HARPS-N plus HIRES RVs that both include a GP activity component whose periodic timescales are constrained to be close to $P_{\text{rot}}/2$ and P_{rot} , respectively. Therefore, we can use our models to conduct a model comparison to assess the favorability of one model over the other. We used the marginalized posterior pdf’s from each model’s MCMC results to estimate their Bayesian model evidences \mathcal{Z} using the estimator from Perrakis et al. (2014). We estimate model evidences of $\ln \mathcal{Z}_1 = -110.0$ and $\ln \mathcal{Z}_2 = -91.0$, which gives a model evidence ratio of $\mathcal{Z}_2/\mathcal{Z}_1 = 10^8$. This result strongly favors the two-planet model, although we caution that Bayesian model evidences are notoriously difficult to accurately calculate and their interpretation is dependent on the assumed model parameter priors (Nelson et al. 2020). Alternatively, we also compute the Bayesian information criterion (BIC) and the Akaike information criterion (AIC) to perform model comparisons that are independent of the

Table 5

Point Estimates of the Hypothetical Planet “c” Keplerian Model Parameters

Parameter	Model Values
Orbital period, P_c (days)	$21.8^{+0.9}_{-0.8}$
Time of midtransit, $T_{0,c}$ (BJD $-2,457,000$)	$1835.3^{+2.2}_{-2.1}$
Log RV semiamplitude, $\ln K_c \text{ m}^{-1} \text{ s}^{-1}$	$1.4^{+0.3}_{-0.5}$
$\sqrt{e_c} \cos \omega_c$	$0.08^{+0.3}_{-0.4}$
$\sqrt{e_c} \sin \omega_c$	$0.12^{+0.37}_{-0.47}$
Derived Parameters	
RV semiamplitude, $K_c \text{ (m s}^{-1}\text{)}$	$4.2^{+1.2}_{-1.7}$
Minimum planet mass, $m_{p,c} \sin i \text{ (} M_{\oplus}\text{)}$	$13.0^{+3.8}_{-5.3}$
Semimajor axis, $a_c \text{ (au)}$	$0.1319^{+0.0046}_{-0.0043}$
Insolation, $F_c \text{ (} F_{\oplus}\text{)}$	$4.6^{+0.6}_{-0.5}$
Equilibrium temperature, $T_{\text{eq},c} \text{ (K)}$	
Bond albedo = 0.0	407 ± 12
Bond albedo = 0.3	373 ± 11

Note. Note that we do not conclude that the hypothetical planet “c” presented in this table is a bona fide planet.

model priors. We measure $\text{BIC}_1 = 225.0$ and $\text{BIC}_2 = 205.2$ such that the two-planet model is again strongly favored since $\Delta\text{BIC}_{12} \equiv \text{BIC}_1 - \text{BIC}_2 = 19.8 > 10$. This is further supported by $\text{AIC}_1 = 202.1$ and $\text{AIC}_2 = 174.1$, whereby the two-planet model remains strongly favored as $\Delta\text{AIC}_{12} \equiv \text{AIC}_1 - \text{AIC}_2 = 28.0 > 10$.

Encouraged by the prospect of a second planet orbiting TOI-1235, we used its measured orbital period $P_c = 21.8^{+0.9}_{-0.8}$ days and its time of inferior conjunction $T_{0,c} = 2, 458, 835.3^{+2.2}_{-2.1}$ BJD to search for transit-like events in the TESS PDCSAP and archival MEarth-North light curves. With TESS we conducted the search for periodic transit-like signals close to P_c using the implementation of the Box Least Squares (BLS) algorithm (Kovács et al. 2002) in Cloutier (2019). We conducted a complementary BLS search on the full MEarth-North light curve following the methods outlined in Ment et al. (2019). We do not find any significant transit-like signals other than those associated with TOI-1235 b. Therefore, if the 22-day signal is truly a planet, then it is unlikely to be transiting. This result is perhaps unsurprising given that if the hypothetical planet “c” is coplanar with TOI-1235 b at 88° , then “c” would not have a transiting configuration at its separation of $a_c/R_s = 45.1^{+2.0}_{-1.9}$.

We emphasize that while the aforementioned lines of evidence are suggestive of a second, nontransiting planet around TOI-1235, the data presented herein are not sufficient to firmly distinguish between planetary and stellar activity origins of the 22-day RV signal. Ongoing spectroscopic monitoring of TOI-1235 over many rotation cycles may help to solve this ambiguity by testing for temporal correlations of the signal’s amplitude over the star’s evolving magnetic activity cycle. A more secure detection of the stellar rotation period from continued photometric monitoring would also be beneficial.

5.4. An Independent Analysis of the TOI-1235 System

Following the announcement of the TOI-1235.01 level-one planet candidate in 2019 October, multiple precision RV instrument teams began pursuing its mass characterization through TFOP. This study has presented the subset of those efforts from HARPS-N and HIRES, but we acknowledge that another collaboration has also submitted a paper presenting

their own RV time series and analysis (Bluhm et al. 2020). Although the submissions of these complementary studies were coordinated between the two groups, their respective data, analyses, and write-ups were intentionally conducted independently.

6. Summary

We have presented the discovery and confirmation of TOI-1235 b, a transiting super-Earth around a bright early M dwarf from the TESS mission. The planet was confirmed through intensive follow-up observations, including a set of precise RV measurements from HARPS-N and HIRES. The main findings of our study are summarized below:

1. TOI-1235 is a bright ($V = 11.495$, $K_s = 7.893$) early M dwarf at 39.6 pc with mass and radius of $0.640 \pm 0.016 M_{\odot}$ and $0.630 \pm 0.015 R_{\odot}$, respectively. Archival MEarth-North photometry reveals a probable rotation period of 44.7 ± 4.5 days.
2. The transiting planet TOI-1235 b has an orbital period of 3.44 days with a mass and radius of $6.91^{+0.75}_{-0.85} M_{\oplus}$ and $1.738^{+0.087}_{-0.076} R_{\oplus}$, respectively. TOI-1235 b directly contributes to the completion of the TESS level-one science requirement to deliver masses for 50 planets with radii $< 4 R_{\oplus}$.
3. Planetary structure models reveal that the TOI-1235 b mass and radius are consistent with an iron mass fraction of $20^{+15}_{-12}\%$ and an H/He envelope mass fraction of $< 0.5\%$ at 90% confidence, therefore making the planet consistent with an Earth-like bulk composition.
4. The period and radius of TOI-1235 b place it between competing model predictions of the location of the rocky/nonrocky planet transition. The rocky composition of TOI-1235 b makes it consistent with thermally driven atmospheric mass-loss scenarios but inconsistent with gas-poor formation models, suggesting that the former physical process is still efficient at sculpting the radius valley around early M dwarfs.
5. We also see a periodic signal in the RV measurements at 22 days, close to the first harmonic of the star’s probable rotation period. While this is suggestive of the signal’s origin being related to stellar activity, estimates of the RV activity signal’s amplitude from photometry and the comparison of one- and two-planet RV models suggest that the signals’ origin may instead be planetary. However, we are unable to definitely distinguish between activity and a second planet with the data presented herein.

R.C. is supported by a grant from the National Aeronautics and Space Administration in support of the TESS science mission. We thank Andrew Vanderburg for enlightening discussions regarding the TESS light curves.

M.P. gratefully acknowledges the support from the European Union Seventh Framework Programme (FP7/2007-2013) under grant agreement No. 313014 (ETAEARTH).

J.M.A.M. gratefully acknowledges support from the National Science Foundation Graduate Research Fellowship Program under grant No. DGE-1842400. J.M.A.M. also thanks the LSSTC Data Science Fellowship Program, which is funded by LSSTC, NSF Cybertraining grant No. 1829740, the Brinson

Foundation, and the Moore Foundation; his participation in the program has benefited this work.

This work has been partially supported by the National Aeronautics and Space Administration under grant No. NNX17AB59G issued through the Exoplanets Research Program.

We acknowledge the use of public TESS Alert data from the pipelines at the TESS Science Office and at the TESS Science Processing Operations Center.

The MEarth Team gratefully acknowledges funding from the David and Lucile Packard Fellowship for Science and Engineering (awarded to D.C.). This material is based on work supported by the National Science Foundation under grants AST-0807690, AST-1109468, AST-1004488 (Alan T. Waterman Award), and AST-1616624. This work is made possible by a grant from the John Templeton Foundation. The opinions expressed in this publication are those of the authors and do not necessarily reflect the views of the John Templeton Foundation. This material is based on work supported by the National Aeronautics and Space Administration under grant No. 80NSSC18K0476 issued through the XRP Program.

This publication makes use of data products from the Two Micron All Sky Survey, which is a joint project of the University of Massachusetts and the Infrared Processing and Analysis Center/California Institute of Technology, funded by the National Aeronautics and Space Administration and the National Science Foundation.

This work has made use of data from the European Space Agency (ESA) mission Gaia (<https://www.cosmos.esa.int/gaia>), processed by the Gaia Data Processing and Analysis Consortium (DPAC, <https://www.cosmos.esa.int/web/gaia/dpac/consortium>). Funding for the DPAC has been provided by national institutions, in particular the institutions participating in the Gaia Multilateral Agreement.

This work makes use of observations from the LCOGT network.

Based on observations made with the Italian Telescopio Nazionale Galileo (TNG) operated by the Fundación Galileo Galilei (FGG) of the Istituto Nazionale di Astrofisica (INAF) at the Observatorio del Roque de los Muchachos (La Palma, Canary Islands, Spain).

The HARPS-N project has been funded by the ProDEX Program of the Swiss Space Office (SSO), the Harvard University Origins of Life Initiative (HUOLI), the Scottish Universities Physics Alliance (SUPA), the University of Geneva, the Smithsonian Astrophysical Observatory (SAO), the Italian National Astrophysical Institute (INAF), the University of St Andrews, Queens University Belfast, and the University of Edinburgh.

Some of the data presented herein were obtained at the W. M. Keck Observatory, which is operated as a scientific partnership among the California Institute of Technology, the University of California, and NASA. The Observatory was made possible by the generous financial support of the W. M. Keck Foundation. The authors wish to recognize and acknowledge the very significant cultural role and reverence that the summit of Maunakea has always had within the indigenous Hawaiian community. We are most fortunate to have the opportunity to conduct observations from this mountain.

Resources supporting this work were provided by the NASA High-End Computing (HEC) Program through the NASA

Advanced Supercomputing (NAS) Division at Ames Research Center for the production of the SPOC data products.









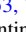
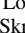
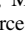

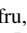
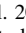




Based on observations obtained at the international Gemini Observatory under the program GN-2019B-LP-101, a program of NSF's OIR Lab, which is managed by the Association of Universities for Research in Astronomy (AURA) under a cooperative agreement with the National Science Foundation on behalf of the Gemini Observatory partnership: the National Science Foundation (United States), National Research Council (Canada), Agencia Nacional de Investigación y Desarrollo (Chile), Ministerio de Ciencia, Tecnología e Innovación (Argentina), Ministério da Ciência, Tecnologia, Inovações e Comunicações (Brazil), and Korea Astronomy and Space Science Institute (Republic of Korea). Some of the observations in the paper made use of the High-Resolution Imaging instrument 'Alopecu'.

Facilities: TESS, MEarth-North, TRES, LCOGT, Gemini/NIRI, TNG/HARPS-N, Keck/HIRES.

Software: AstroImageJ (Collins et al. 2017), astropy (Astropy Collaboration et al. 2013, 2018), BANZAI (McCully et al. 2018), batman (Kreidberg 2015), BGLS (Mortier et al. 2015), celerite (Foreman-Mackey et al. 2017), emcee (Foreman-Mackey et al. 2013), EvapMass (Owen & Campos Estrada 2020), EXOFAST (Eastman et al. 2013), EXOFASTv2 (Eastman et al. 2019), exoplanet (Foreman-Mackey et al. 2019), PyMC3 (Salvatier et al. 2016), scipy (Virtanen et al. 2020), SpecMatch-Emp (Yee et al. 2017), STARRY (Luger et al. 2019), Tapir (Jensen 2013), TERRA (Anglada-Escudé & Butler 2012), triceratops (Giacalone & Dressing 2020), vespa (Morton 2012).

ORCID iDs

Ryan Cloutier  <https://orcid.org/0000-0001-5383-9393>
 Joseph E. Rodriguez  <https://orcid.org/0000-0001-8812-0565>
 David Charbonneau  <https://orcid.org/0000-0002-9003-484X>
 Keivan G. Stassun  <https://orcid.org/0000-0002-3481-9052>
 Annelies Mortier  <https://orcid.org/0000-0001-7254-4363>
 David W. Latham  <https://orcid.org/0000-0001-9911-7388>
 Howard Isaacson  <https://orcid.org/0000-0002-0531-1073>
 Andrew W. Howard  <https://orcid.org/0000-0001-8638-0320>
 Stéphane Udry  <https://orcid.org/0000-0001-7576-6236>
 Karen A. Collins  <https://orcid.org/0000-0001-6588-9574>
 Allyson Beiryla  <https://orcid.org/0000-0001-6637-5401>
 Gilbert A. Esquerdo  <https://orcid.org/0000-0002-9789-5474>
 Elisabeth Matthews  <https://orcid.org/0000-0003-0593-1560>
 Rachel A. Matson  <https://orcid.org/0000-0001-7233-7508>
 Steve B. Howell  <https://orcid.org/0000-0002-2532-2853>
 Jennifer G. Winters  <https://orcid.org/0000-0001-6031-9513>
 Chantanelle Nava  <https://orcid.org/0000-0001-8838-3883>
 Kristo Ment  <https://orcid.org/0000-0001-5847-9147>
 George Ricker  <https://orcid.org/0000-0003-2058-6662>
 Roland Vanderspek  <https://orcid.org/0000-0001-6763-6562>
 Sara Seager  <https://orcid.org/0000-0002-6892-6948>
 Jon M. Jenkins  <https://orcid.org/0000-0002-4715-9460>
 Eric B. Ting  <https://orcid.org/0000-0002-8219-9505>
 Peter Tenenbaum  <https://orcid.org/0000-0002-1949-4720>
 Alessandro Sozzetti  <https://orcid.org/0000-0002-7504-365X>

- Lizhou Sha  <https://orcid.org/0000-0001-5401-8079>
 Damien Ségransan  <https://orcid.org/0000-0003-2355-8034>
 Joshua E. Schlieder  <https://orcid.org/0000-0001-5347-7062>
 Dimitar Sasselov  <https://orcid.org/0000-0001-7014-1771>
 Arpita Roy  <https://orcid.org/0000-0001-8127-5775>
 Paul Robertson  <https://orcid.org/0000-0003-0149-9678>
 Ennio Poretti  <https://orcid.org/0000-0003-1200-0473>
 Giampaolo Piotto  <https://orcid.org/0000-0002-9937-6387>
 Joshua Pepper  <https://orcid.org/0000-0002-3827-8417>
 Emilio Molinari  <https://orcid.org/0000-0002-1742-7735>
 Teo Mocnik  <https://orcid.org/0000-0003-4603-556X>
 Giuseppina Micela  <https://orcid.org/0000-0002-9900-4751>
 Jack Lubin  <https://orcid.org/0000-0001-8342-7736>
 Mercedes López-Morales  <https://orcid.org/0000-0003-3204-8183>
 John F. Kielkopf  <https://orcid.org/0000-0003-0497-2651>
 Stephen R. Kane  <https://orcid.org/0000-0002-7084-0529>
 Eric L. N. Jensen  <https://orcid.org/0000-0002-4625-7333>
 Daniel Huber  <https://orcid.org/0000-0001-8832-4488>
 Michelle L. Hill <https://orcid.org/0000-0002-0139-4756>
 Steven Giacalone <https://orcid.org/0000-0002-8965-3969>
 Adriano Ghedina <https://orcid.org/0000-0003-4702-5152>
 Xavier Dumusque <https://orcid.org/0000-0002-9332-2011>
 Courtney D. Dressing <https://orcid.org/0000-0001-8189-0233>
 Paul A. Dalba <https://orcid.org/0000-0002-4297-5506>
 Rosario Cosentino <https://orcid.org/0000-0003-1784-1431>
 Dennis M. Conti <https://orcid.org/0000-0003-2239-0567>
 Knicole D. Colón <https://orcid.org/0000-0001-8020-7121>
 Kevin I. Collins <https://orcid.org/0000-0003-2781-3207>
 David Ciardi <https://orcid.org/0000-0002-5741-3047>
 Jessie Christiansen <https://orcid.org/0000-0002-8035-4778>
 Ashley Chontos <https://orcid.org/0000-0003-1125-2564>
 Douglas A. Caldwell <https://orcid.org/0000-0003-1963-9616>
 Christopher Burke <https://orcid.org/0000-0002-7754-9486>
 Lars Buchhave <https://orcid.org/0000-0003-1605-5666>
 Aida Behmard <https://orcid.org/0000-0003-0012-9093>
 Corey Beard <https://orcid.org/0000-0001-7708-2364>
 Joseph M. Akana Murphy <https://orcid.org/0000-0001-8898-8284>
- References**
- Aigrain, S., Pont, F., & Zucker, S. 2012, *MNRAS*, 419, 3147
 Ambikasaran, S., Foreman-Mackey, D., Greengard, L., Hogg, D. W., & O’Neil, M. 2014, arXiv:1403.6015
 Anglada-Escudé, G., & Butler, R. P. 2012, *ApJS*, 200, 15
 Ansdell, M., Gaidos, E., Mann, A. W., et al. 2015, *ApJ*, 798, 41
 Astropy Collaboration, Price-Whelan, A. M., Sipőcz, B. M., et al. 2018, *AJ*, 156, 123
 Astropy Collaboration, Robitaille, T. P., Tollerud, E. J., et al. 2013, *A&A*, 558, A33
 Astudillo-Defru, N., Cloutier, R., Wang, S. X., et al. 2020, *MNRAS*, 493, 792
 Bedell, M., Bean, J. L., Meléndez, J., et al. 2018, *ApJ*, 865, 68
 Benedict, G. F., Henry, T. J., Franz, O. G., et al. 2016, *AJ*, 152, 141
 Berta, Z. K., Irwin, J., Charbonneau, D., Burke, C. J., & Falco, E. E. 2012, *AJ*, 144, 145
 Bianchi, L., Shiao, B., & Thilker, D. 2017, *ApJS*, 230, 24
 Bluhm, P., Luque, R., Espinoza, N., et al. 2020, arXiv:2004.06218
 Bonfils, X., Almenara, J.-M., Cloutier, R., et al. 2018, *A&A*, 618, A142
 Bonfils, X., Gillon, M., Udry, S., et al. 2012, *A&A*, 546, A27
 Brown, T. M., Baliber, N., Bianco, F. B., et al. 2013, *PASP*, 125, 1031
 Charbonneau, D., Berta, Z. K., Irwin, J., et al. 2009, *Natur*, 462, 891
 Chen, H., & Rogers, L. A. 2016, *ApJ*, 831, 180
 Ciardi, D. R., Beichman, C. A., Horch, E. P., & Howell, S. B. 2015, *ApJ*, 805, 16
 Claret, A., & Bloemen, S. 2011, *A&A*, 529, A75
 Cloutier, R. 2019, *AJ*, 158, 81
 Cloutier, R., Astudillo-Defru, N., Bonfils, X., et al. 2019a, *A&A*, 629, A111
 Cloutier, R., Astudillo-Defru, N., Doyon, R., et al. 2019b, *A&A*, 621, A49
 Cloutier, R., Eastman, J. D., Rodriguez, J. E., et al. 2020, arXiv:2003.01136
 Cloutier, R., & Menou, K. 2020, *AJ*, 159, 211
 Collins, K. A., Kielkopf, J. F., Stassun, K. G., & Hessman, F. V. 2017, *AJ*, 153, 77
 Cosentino, R., Lovis, C., Pepe, F., et al. 2012, *Proc. SPIE*, 8446, 84461V
 Cutri, R. M., Skrutskie, M. F., van Dyk, S., et al. 2003, 2MASS All Sky Catalog of Point Sources (Washington, DC: NASA)
 Cutri, R. M. 2013, yCat, 2328, 0
 Damasso, M., Bonomo, A. S., Astudillo-Defru, N., et al. 2018, *A&A*, 615, A69
 Dittmann, J. A., Irwin, J. M., Charbonneau, D., et al. 2017, *Natur*, 544, 333
 Dressing, C. D., Charbonneau, D., Dumusque, X., et al. 2015, *ApJ*, 800, 135
 Dumusque, X., Boisse, I., & Santos, N. C. 2014, *ApJ*, 796, 132
 Eastman, J., Gaudi, B. S., & Agol, E. 2013, *PASP*, 125, 83
 Eastman, J. D., Rodriguez, J. E., Agol, E., et al. 2019, arXiv:1907.09480
 Evans, D. W., Riello, M., de Angeli, F., et al. 2018, *A&A*, 616, A4
 Foreman-Mackey, D., Agol, E., Ambikasaran, S., & Angus, R. 2017, *AJ*, 154, 220
 Foreman-Mackey, D., Barentsen, G., & Barclay, T. 2019, dfm/exoplanet: exoplanet v0.1.6, Zenodo, doi:10.5281/zenodo.2651251
 Foreman-Mackey, D., Hogg, D. W., Lang, D., & Goodman, J. 2013, *PASP*, 125, 306
 Fortney, J. J., Marley, M. S., & Barnes, J. W. 2007, *ApJ*, 659, 1661
 France, K., Froning, C. S., Linsky, J. L., et al. 2013, *ApJ*, 763, 149
 Fulton, B. J., & Petigura, E. A. 2018, *AJ*, 156, 264
 Fulton, B. J., Petigura, E. A., Howard, A. W., et al. 2017, *AJ*, 154, 109
 Gaia Collaboration, Brown, A. G. A., Vallenari, A., et al. 2018, *A&A*, 616, A1
 Giacalone, S., & Dressing, C. D. 2020, arXiv:2002.00691
 Ginzburg, S., Schlichting, H. E., & Sari, R. 2016, *ApJ*, 825, 29
 Ginzburg, S., Schlichting, H. E., & Sari, R. 2018, *MNRAS*, 476, 759
 Gupta, A., & Schlichting, H. E. 2019, *MNRAS*, 487, 24
 Gupta, A., & Schlichting, H. E. 2020, *MNRAS*, 493, 792
 Hauschildt, P. H., Allard, F., Ferguson, J., Baron, E., & Alexander, D. R. 1999, *ApJ*, 525, 871
 Hodapp, K. W., Jensen, J. B., Irwin, E. M., et al. 2003, *PASP*, 115, 1388
 Høg, E., Fabricius, C., Makarov, V. V., et al. 2000, *A&A*, 355, L27
 Howard, A. W., Johnson, J. A., Marcy, G. W., et al. 2010, *ApJ*, 721, 1467
 Howell, S. B., Everett, M. E., Sherry, W., Horch, E., & Ciardi, D. R. 2011, *AJ*, 142, 19
 Irwin, J., Aigrain, S., Hodgkin, S., et al. 2006, *MNRAS*, 370, 954
 Irwin, J., Berta, Z. K., Burke, C. J., et al. 2011, *ApJ*, 727, 56
 Irwin, J. M., Berta-Thompson, Z. K., Charbonneau, D., et al. 2015, in 18th Cambridge Workshop on Cool Stars, Stellar Systems, and the Sun, ed. G. T. van Belle & H. C. Harris, 767
 Jenkins, J. M. 2002, *ApJ*, 575, 493
 Jenkins, J. M., Chandrasekaran, H., McCauliff, S. D., et al. 2010, *Proc. SPIE*, 7740, 77400D
 Jenkins, J. M., Twicken, J. D., McCauliff, S., et al. 2016, *Proc. SPIE*, 9913, 99133E
 Jensen, E. 2013, Tapir: A Web Interface for Transit/Eclipse Observability, Astrophysics Source Code Library, ascl:1306.007
 Jin, S., & Mordasini, C. 2018, *ApJ*, 853, 163
 Jin, S., Mordasini, C., Parmentier, V., et al. 2014, *ApJ*, 795, 65
 Kipping, D. M. 2013, *MNRAS*, 434, L51
 Kovács, G., Zucker, S., & Mazeh, T. 2002, *A&A*, 391, 369
 Kreidberg, L. 2015, *PASP*, 127, 1161
 Kurucz, R. L. 2013, ATLAS12: Opacity Sampling Model Atmosphere Program, Astrophysics Source Code Library, ascl:1303.024
 Lee, E. J., & Chiang, E. 2015, *ApJ*, 811, 41
 Lee, E. J., & Chiang, E. 2016, *ApJ*, 817, 90
 Lee, E. J., Chiang, E., & Ormel, C. W. 2014, *ApJ*, 797, 95
 Li, J., Tenenbaum, P., Twicken, J. D., et al. 2019, *PASP*, 131, 024506
 Lindegren, L., Hernández, J., Bombrun, A., et al. 2018, *A&A*, 616, A2
 Lodders, K. 2003, *ApJ*, 591, 1220
 Lopez, E. D., & Fortney, J. J. 2013, *ApJ*, 776, 2
 Lopez, E. D., & Fortney, J. J. 2014, *ApJ*, 792, 1
 Lopez, E. D., Fortney, J. J., & Miller, N. 2012, *ApJ*, 761, 59
 Lopez, E. D., & Rice, K. 2018, *MNRAS*, 479, 5303
 Lovis, C., & Pepe, F. 2007, *A&A*, 468, 1115
 Luger, R., Agol, E., Foreman-Mackey, D., et al. 2019, *AJ*, 157, 64
 Luque, R., Pallé, E., Kossakowski, D., et al. 2019, *A&A*, 628, A39

- Mandel, K., & Agol, E. 2002, *ApJL*, **580**, L171
- Mann, A. W., Feiden, G. A., Gaidos, E., Boyajian, T., & von Braun, K. 2015, *ApJ*, **804**, 64
- Marcus, R. A., Sasselov, D., Hernquist, L., & Stewart, S. T. 2010, *ApJL*, **712**, L73
- Martinez, C. F., Cunha, K., Ghezzi, L., & Smith, V. V. 2019, *ApJ*, **875**, 29
- Mayo, A. W., Vanderburg, A., Latham, D. W., et al. 2018, *AJ*, **155**, 136
- McCully, C., Volgenau, N. H., Harbeck, D.-R., et al. 2018, *Proc. SPIE*, **10707**, 107070K
- Ment, K., Dittmann, J. A., Astudillo-Defru, N., et al. 2019, *AJ*, **157**, 32
- Milbourne, T. W., Haywood, R. D., Phillips, D. F., et al. 2019, *ApJ*, **874**, 107
- Mortier, A., & Collier Cameron, A. 2017, *A&A*, **601**, A110
- Mortier, A., Faria, J. P., Correia, C. M., Santerne, A., & Santos, N. C. 2015, *A&A*, **573**, A101
- Morton, T. D. 2012, *ApJ*, **761**, 6
- Muirhead, P. S., Dressing, C. D., Mann, A. W., et al. 2018, *AJ*, **155**, 180
- Nava, C., López-Morales, M., Haywood, R. D., & Giles, H. A. C. 2020, *AJ*, **159**, 23
- Nelson, B. E., Ford, E. B., Buchner, J., et al. 2020, *AJ*, **159**, 73
- Newton, E. R., Irwin, J., Charbonneau, D., et al. 2016, *ApJ*, **821**, 93
- Newton, E. R., Irwin, J., Charbonneau, D., et al. 2017, *ApJ*, **834**, 85
- Nowak, G., Luque, R., Parviainen, H., et al. 2020, arXiv:2003.01140
- Nutzman, P., & Charbonneau, D. 2008, *PASP*, **120**, 317
- Owen, J. E., & Campos Estrada, B. 2020, *MNRAS*, **491**, 5287
- Owen, J. E., & Wu, Y. 2013, *ApJ*, **775**, 105
- Owen, J. E., & Wu, Y. 2017, *ApJ*, **847**, 29
- Perrakis, K., Ntzioufras, I., & Tsonas, E. G. 2014, *Comput. Stat. Data Anal.*, **77**, 54
- Rafikov, R. R. 2006, *ApJ*, **648**, 666
- Reid, I. N., Kilkeny, D., & Cruz, K. L. 2002, *AJ*, **123**, 2822
- Reiners, A., Bean, J. L., Huber, K. F., et al. 2010, *ApJ*, **710**, 432
- Ricker, G. R., Winn, J. N., Vanderspek, R., et al. 2015, *JATIS*, **1**, 014003
- Rogers, L. A. 2015, *ApJ*, **801**, 41
- Salvatier, J., Wiecki, T. V., & Fonnesbeck, C. 2016, *PeerJ Computer Science*, **2**, e55
- Shporer, A., Collins, K. A., Astudillo-Defru, N., et al. 2020, *ApJL*, **890**, L7
- Smith, J. C., Stumpe, M. C., van Cleve, J. E., et al. 2012, *PASP*, **124**, 1000
- Stassun, K. G., Collins, K. A., & Gaudi, B. S. 2017, *AJ*, **153**, 136
- Stassun, K. G., Corsaro, E., Pepper, J. A., & Gaudi, B. S. 2018a, *AJ*, **155**, 22
- Stassun, K. G., Oelkers, R. J., Paegert, M., et al. 2019, *AJ*, **158**, 138
- Stassun, K. G., Oelkers, R. J., Pepper, J., et al. 2018b, *AJ*, **156**, 102
- Stassun, K. G., & Torres, G. 2016, *AJ*, **152**, 180
- Stassun, K. G., & Torres, G. 2018, *ApJ*, **862**, 61
- Stelzer, B., Damasso, M., Scholz, A., & Matt, S. P. 2016, *MNRAS*, **463**, 1844
- Stumpe, M. C., Smith, J. C., Catanzarite, J. H., et al. 2014, *PASP*, **126**, 100
- Stumpe, M. C., Smith, J. C., van Cleve, J. E., et al. 2012, *PASP*, **124**, 985
- Twicken, J. D., Catanzarite, J. H., Clarke, B. D., et al. 2018, *PASP*, **130**, 064502
- Valencia, D., O'Connell, R. J., & Sasselov, D. D. 2007, *ApJL*, **670**, L45
- van Eylen, V., Agentoft, C., Lundkvist, M. S., et al. 2018, *MNRAS*, **479**, 4786
- Virtanen, P., Gommers, R., Oliphant, T. E., et al. 2020, *Nat. Methods*, **17**, 261
- Vogt, S. S., Allen, S. L., Bigelow, B. C., et al. 1994, *Proc. SPIE*, **2198**, 362
- Walkowicz, L. M., Johns-Krull, C. M., & Hawley, S. L. 2008, *ApJ*, **677**, 593
- Weiss, L. M., & Marcy, G. W. 2014, *ApJL*, **783**, L6
- Wright, N. J., Drake, J. J., Mamajek, E. E., & Henry, G. W. 2011, *ApJ*, **743**, 48
- Wu, Y. 2019, *ApJ*, **874**, 91
- Yee, S. W., Petigura, E. A., & von Braun, K. 2017, *ApJ*, **836**, 77
- York, D. G., Adelman, J., Anderson, J. E. J., et al. 2000, *AJ*, **120**, 1579
- Zeng, L., Jacobsen, S. B., Sasselov, D. D., et al. 2019, *PNAS*, **116**, 9723
- Zeng, L., & Sasselov, D. 2013, *PASP*, **125**, 227